

Combustion Theory and Modelling
Vol. 00, No. 00, Month 200x, 1–35

RESEARCH ARTICLE

On Turbulent Chemical Explosions Into Dilute Aluminum Particle Clouds

K. Balakrishnan and S. Menon*
School of Aerospace Engineering,
Georgia Institute of Technology,
Atlanta, GA, 30332-0150, USA

(Submitted: January, 2010)

Total Word Count: \sim 12,400 words

*Corresponding author. Phone: 404-894-9126; Email: suresh.menon@aerospace.gatech.edu

Abstract

We use a hybrid two-phase numerical methodology to investigate the flow-field subsequent to the detonation of a spherical charge of TNT with an ambient distribution of a dilute cloud of aluminum particles. Rayleigh-Taylor instability ensues on the contact surface that separates the inner detonation products and the outer shock-compressed air due to inter-phase interaction, which grows in time and results in a mixing layer where the detonation products afterburn with the air. At early times, the ambient particles are completely engulfed into the detonation products, where they pick up heat and ignite, pick up momentum and disperse. Subsequently, as they disperse radially outwards, they interact with the temporally growing Rayleigh-Taylor structures, and the vortex rings around the hydrodynamic structures results in the clustering of the particles by also introducing local transverse dispersion. Then the particles leave the mixing layer and quench, yet preserve their hydrodynamic “foot print” even until much later; due to this clustering, preferential heating and combustion of particles is observed. With a higher initial mass loading in the ambient cloud, larger clusters are observed due to stronger/larger hydrodynamic structures in the mixing layer—a direct consequence of more particles available to perturb the contact surface initially. With a larger particle size in the initial cloud, clustering is not observed, but when the initial cloud is wider, fewer and degenerate clusters are observed. We identify five different phases in the dispersion of the particles: (1) engulfment phase; (2) hydrodynamic instability-interaction phase; (3) first vortex-free dispersion phase; (4) reshock phase; and (5) second vortex-free dispersion phase. Finally, a theoretical Buoyancy-Drag model is used to predict the growth pattern of the “bubbles” and is in agreement with the simulation results. Overall, this study has provided some useful insights on the post-detonation explosive dispersal of dilute aluminum particle clouds.

Keywords: Explosive, Mixing Layer, Aluminum Combustion, Clustering, Dispersion, Rayleigh-Taylor Instability

1. Introduction

Explosives are ubiquitous in many engineering industries and have applications in mining, in modern warfare, to quench fires in the oil industry, etc. Although explosions have been widely studied by the research community for well over a century, many phenomena still remain to be investigated in order to properly understand and characterize the flow-field in the post-detonation regime. In particular, the characterization of explosions into ambient solid non-reactive or reactive particles has not been previously addressed to detail. For instance, ambient aluminum (or any other material) particles can perturb the flow-field behind the leading blast wave, ensuing in hydrodynamic instabilities that can grow with time. Hydrodynamic instabilities such as Rayleigh-Taylor and Richtmyer-Meshkov have been shown to occur in the flow-field behind blast waves [1–3, 20, 21]. Experimental studies to understand these flow physics are very difficult due to the hostile, short-lived environment behind explosive blast waves; thus, investigations based on computational simulations, such as the present one, offer wider leverage to properly understand and characterize the flow-field in the post-detonation regime of a high explosive, particularly when ambient reactive particles like aluminum are present.

Two of the earliest studies of blast waves from intense explosions were carried out independently by Taylor [37] and Sedov [34], and are seminal in the field. These studies are primarily one-dimensional explosions, which is generally not the case in most real explosions, especially the flow-field behind the blast wave. When a spherical (or cylindrical) charge of a high explosive such as Trinitrotoluene (TNT) or nitromethane (NM) is detonated, a blast wave propagates outwards after the detonation wave consumes all the high explosive; this blast wave attenuates and decelerates with time due to spherical spreading. The contact surface that separates the inner detonation products and the outer shock-compressed air also propagates outwards as the detonation products expand. At the same time, a rarefaction wave propagates inwards from the outer boundary of the charge, subsequently over-expanding the flow near the core of the charge. This over-expansion creates a secondary shock that is initially swept outwards, subsequently implodes inwards

and, later, explodes outwards again after reflection from the origin [7]. To better illustrate the physics of explosions, in particular when a ring of solid particles are present surrounding the explosive charge, a schematic of the primary and secondary shocks, the contact surface, and the dispersing particle cloud are presented in Figure 1, albeit from a one-dimensional sense.

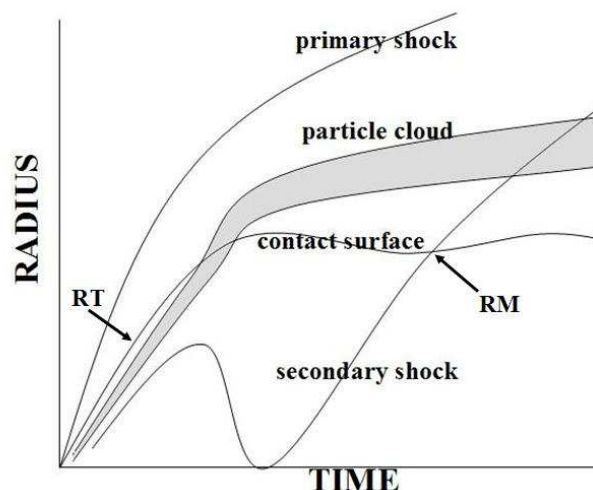


Figure 1. Radius-time diagram of the one-dimensional post-detonation flow-field. Note: this is a schematic only.

Concomitant to these processes is the interaction of the contact surface with ambient particles, if present. Recent experimental studies of Shock-Dispersed Fuel (SDF) charges [22, 43], i.e., charges of a high explosive surrounded with a shell of aluminum particles, have shown that significant amounts of afterburn, both of the detonation products as well as the aluminum, results in increased impulse. If ambient particles are too small and/or light, the leading blast wave may rapidly set them into motion and they may never interact with the contact surface. This is particularly true apropos of blast waves propagating into a cloud of liquid droplets [33]. On the other hand, if the particles are sufficiently large and/or heavy, the leading blast wave may not impart a significant enough momentum to the particles, thus allowing for the contact surface to overtake the particles. Then, the particles pick up momentum, are set into motion, and catch up with the contact surface [2]. Thus, for sufficiently large and/or heavy particles, the contact-surface interaction with particles occurs twice—first time when the contact surface overtakes the particles, and second time when the particles again overtake the contact surface. Since particles are inevitably randomly distributed in a realistic cloud, perturbations to the contact surface may occur at various locations and hence trigger instabilities at multiple wavelengths. These perturbations can grow in time into Rayleigh-Taylor instability [38] owing to the high density ratio (~ 500 -1000) across the contact surface at early times; since the perturbations/instabilities are random, i.e., they have different wavelengths, they will grow at different rates [8]. In Figure 1, ‘RT’ denotes the instant when Rayleigh-Taylor instability grows on the contact surface.

The Rayleigh-Taylor instability grows as “bubbles” of lighter fluid “rising” into the heavier fluid, and “spikes” of heavier fluid “falling” into the lighter fluid [23, 28, 29]. Thus, the early-phase mixing is primarily macroscopic in the sense that large-scale intrusions of one fluid into the other occurs. Since explosions inevitably involve very high density ratios between the high and low density fluids,

i.e., Atwood number ($A = \frac{\rho_h - \rho_l}{\rho_h + \rho_l}$, where ρ_h and ρ_l denote respectively the densities of the high and low density fluids) close to unity, the bubbles are significantly larger in transverse scale than the spikes. These bubbles exist at multiple sizes and wavelengths, and so with time larger bubbles easily overtake the volume occupied by their smaller counterparts, thereby engulfing them. This results in a “bubble competition” [23, 28, 29] where contiguous bubbles interact and merge, giving rise to larger scale structures. This competition can also involve between bubbles of different generations [28, 29], i.e., smaller bubbles can compete, merge and, subsequently, the merged larger bubbles can again compete and merge. Miles and co-workers [28, 29] classify this bubble merging as an inverse cascade process, as kinetic energy is transferred from smaller bubbles (or smaller scales) to larger ones; this merging can lead to a loss of memory of the initial perturbations and an acceleration of the bubble front. Due to bubble merging, the total number of hydrodynamic structures decreases with time, but their size increases. This results in a mixing layer, i.e., a finite region of space where the inner detonation products mix with the outer air and burn, accompanied with the release of afterburning energy [1, 2, 20, 21]. The mixing layer grows in time and convects downstream due to flow expansion, with the boundaries asymptoting at late times. Finally, once sufficiently large enough scales have been reached, no further bubble merging occurs, and self-similar growth of the Rayleigh-Taylor structures is possible.

Subsequent to the aforementioned phenomena, the secondary shock, during its outward passage, interacts with the hydrodynamic structures in the mixing layer, a phenomena that gives rise to a Richtmyer-Meshkov instability [32]. Here, vorticity is created by the baroclinic mechanism, and this sustains the mixing process at later times [1, 2, 20]. In Figure 1, ‘RM’ denotes the instant when Richtmyer-Meshkov instability occurs on the contact surface/mixing layer. Particles when present in the detonation of a high explosive, either inside or outside the charge, enhance the mixing process, which in turn releases energy in addition to the detonation energy. This energy release results in increased temperature and volumetric expansion, which can play a role in the subsequent mixing process and hydrodynamic instability growth.

Although the large and/or heavy particles interact with the contact surface twice, the first and second interactions may not be of similar proportions due to several reasons. First, the particle to gas velocity difference and the gas densities are different during the first and second interactions, as the flow expands. Second, when the ambient particles are reactive (say, aluminum), they can ignite subsequent to the first interaction, and can significantly burn, thereby the particles are smaller in size during the second interaction. In addition, since the second particle-contact surface interaction occurs radially farther than the first (as the mixing layer is convected downstream), even the spacing between contiguous particles is now increased. Thus, the second interaction is not as significant as the first in terms of the amount of mixing introduced to the gas-phase. However, this second interaction can be significant to the dispersion characteristics of the particle phase, as we will show in this paper. Subsequently, the particles by virtue of their higher inertia than the gas, slow down less and then leave the mixing layer. We have recently shown that ambient aluminum particles enhance mixing between the detonation products and the air [2], with the following conclusions with regard to mixing and afterburn: (1) the amount of mixing is nearly independent of the particle size; (2) mixing is enhanced when the mass loading ratio, η (defined as the ratio of the mass of the solid to the mass of the gas in a given volume) of the particles is higher; and (3) mixing is enhanced when the initial radial extent of the outer particle cloud is wider. Furthermore, we also showed in [2] that aluminum

particle ignition due to an explosive blast wave is related to the amount of mixing and afterburn energy release, i.e., the mixing aspects of the detonation products and air plays a central role in the sustenance of burning of the aluminum particles. Moreover, the aluminum particles quench as they leave the mixing layer due to the surroundings being relatively ‘cooler’ and the amount of aluminum that remains after the quenching is also related to the amount of mixing and afterburn [2]. In [2], we explored aluminum particles of $10\ \mu\text{m}$ radius and higher; here, the focus is on 5 and $10\ \mu\text{m}$ particle radius clouds, as these smaller size particles have faster momentum response time scales, and can thus “respond” to the vortex rings around the hydrodynamic structures in the mixing layer.

Depending on the size of the aluminum particles, they can ignite either when present in the mixing layer, or when completely engulfed into the detonation products, or when present in the outer air. Since the availability of heat and the choice of the oxidizer are different in these three regions, so is expected their ignition and burning characteristics; the burning can be aerobic (O_2 controlled) or anaerobic (CO_2 or H_2O controlled) [19]. Furthermore, if the particles ignite in the mixing layer, there can be a competition between aluminum and the C and CO of the detonation products for the limited availability of the oxidizer(s)—this is still unknown to the research community. The other challenge pertains to the different combustion regimes of aluminum particles. Aluminum particle combustion can occur in the diffusive or the kinetic regimes [36, 40]. In the diffusive regime, aluminum evaporates and the aluminum gas diffuses farther away from the particle surface until it encounters an oxidizer to burn; here, the diffusion flame is far from the particle surface. On the contrary, in the kinetic regime, the oxidizer diffuses to the surface faster, resulting in chemical reaction near to the particle surface. Thus, the two regimes are very different in the physical phenomena that govern them, resulting in different burn time predictions. The interested reader is referred to more elaborate theoretical discussions on aluminum particle combustion regimes elsewhere [36, 40]. One of the primary distinctions between the two regimes is the burn time—theoretically, it scales as d^2 for the diffusive regime, and as d for the kinetic regime, where d denotes the particle diameter. The diffusive regime of aluminum particle combustion has been more widely used by the research community with the correlation provided by [5] and the references therein. However, recent experimental shock tube data of small aluminum particles ($3\text{--}11\ \mu\text{m}$ dia.) shows that the burning of aluminum is very different in different oxidizers and is also pressure dependent [4, 25], conforming to the kinetic regime. Another research group [36] has also shown that the kinetic regime is more appropriate for aluminum particle combustion in post-detonation events.

In addition to the ignition and combustion issues, the dispersion of a cloud of solid particles is also of preponderant interest. In a mixing layer, where heat and/or oxidizer availability are not uniformly distributed, dispersion of particles can play a central role in the ignition and the subsequent combustion process. For, dispersion can either enable particles to concentrate in regions with surplus heat and/or oxidizer, or can carry them away; thus, dispersion may either assist in the ignition and combustion of the aluminum particles, or may be detrimental to the same. Evidence from computational simulations outlined in [2] clearly demonstrate the preponderance of the mixing-controlled afterburn energy release on the ignition and the sustenance of burning of aluminum particles; thus, dispersion of particles (which cannot be accurately predicted from one-dimensional simulations) is critical to the problem under study. Particle dispersion can also result in clustering effects due to transverse dispersion, which is also of interest in the current investigation. The study of dispersion and ignition of aluminum particles by ex-

plosive blast waves and their interaction with hydrodynamic instabilities is still in its infancy, and requires more elaborate studies—this paper is aimed to provide some useful insights along these lines. These studies have applications to explosive dispersal of reactive metal particles—also termed as Shock-Dispersed Fuel (SDF) charges [22, 43]—where hydrodynamic instabilities can play a significant role in the amount of late time mixing and afterburn. Insights on the physics of particle dispersion due to their interaction with hydrodynamic instabilities can be directly applied for investigations of SDF charges.

The main objectives of this paper are to understand the interaction of an ambient cloud of aluminum particles and the contact surface during the post-detonation flow-field of a TNT explosive charge. The ignition, combustion, and clustering effects of the particle cloud are studied in detail and explained. This paper is organized as follows: in Section 2, we present the governing equations and the numerical methodology; in Section 3, the results from the current study are reported and the involved physics elucidated; finally, in Section 4, the conclusions drawn from this research effort are presented.

2. Governing Equations and Numerical Method

2.1 Gas Phase

We use Large Eddy Simulation (LES) methodology of the compressible, unsteady, multiphase gas phase equations using a finite-volume method [14, 27]. Since the flow field is dilute in nature, the entire volume is exclusively made available to the gas, i.e., we neglect the solid volume fraction. The favre-filtered gas-phase governing equations are summarized as follows [14, 27]:

$$\frac{\partial \bar{\rho}}{\partial t} + \frac{\partial \bar{\rho} \tilde{u}_i}{\partial x_i} = \tilde{\rho}_s, \quad (1)$$

$$\frac{\partial \bar{\rho} \tilde{u}_i}{\partial t} + \frac{\partial}{\partial x_j} [\bar{\rho} \tilde{u}_i \tilde{u}_j + \bar{P} \delta_{ij} - \bar{\tau}_{ij} + \tau_{ij}^{sgs}] = \widetilde{F_{s,i}}, \quad (2)$$

$$\frac{\partial \bar{\rho} \tilde{E}}{\partial t} + \frac{\partial}{\partial x_j} [\bar{\rho} \tilde{u}_j \tilde{E} + \tilde{u}_j \bar{P} + \bar{q}_j - \tilde{u}_i \bar{\tau}_{ji} + H_j^{sgs} + \sigma_j^{sgs}] = \widetilde{Q_s} + \widetilde{W_s}, \quad (3)$$

$$\frac{\partial \bar{\rho} \tilde{Y}_k}{\partial t} + \frac{\partial}{\partial x_i} [\bar{\rho} (\tilde{Y}_k \tilde{u}_i + \tilde{Y}_k \tilde{V}_{i,k}) + Y_{i,k}^{sgs} + \theta_{i,k}^{sgs}] = \dot{\omega}_k + \widetilde{S_{s,k}}, \quad (4)$$

for the continuity, momentum, energy and k -th species equations, respectively. The tilde (\sim) denotes the resolved scale, and the overbar represents a spatial filtering; the variables denote the usual flow parameters [14, 27]. The terms with the superscript sgs represent the sub-grid terms, and appropriate closures are used to model them [14, 27]. These terms are identified as the sub-grid stress tensor τ_{ij}^{sgs} , sub-grid total enthalpy H_j^{sgs} , sub-grid convective species flux $Y_{i,k}^{sgs}$, sub-grid viscous work σ_j^{sgs} , and sub-grid diffusive transport $\theta_{i,k}^{sgs}$ [14, 27]. To close these terms, we solve the sub-grid kinetic energy (k^{sgs}) equation:

$$\frac{\partial}{\partial t} \bar{\rho} k^{sgs} + \frac{\partial}{\partial x_i} (\bar{\rho} \tilde{u}_i k^{sgs}) = -\tau_{ij}^{sgs} \frac{\partial \tilde{u}_i}{\partial x_j} + P_{k^{sgs}} - D_{k^{sgs}}. \quad (5)$$

$P_{k^{sgs}}$ and $D_{k^{sgs}}$ denote respectively, the production and dissipation of k^{sgs} , obtained as:

$$P_{k^{sgs}} = \frac{\partial}{\partial x_i} \left(\bar{\rho} \nu_t \frac{\partial k^{sgs}}{\partial x_i} \right); D_{k^{sgs}} = C_\epsilon \bar{\rho} \frac{(k^{sgs})^{1.5}}{\Delta}. \quad (6)$$

Here, ν_t represents the sub-grid eddy viscosity, and is modeled as $\nu_t = C_\nu \Delta \sqrt{k^{sgs}}$, where Δ is computed using the local grid size as $\Delta = (\Delta x \Delta y \Delta z)^{1/3}$. The constants C_ν and C_ϵ are set values of 0.067 and 0.916, respectively [27]. The sub-grid stress tensor is obtained as

$$\tau_{ij}^{sgs} = -2\bar{\rho} \nu_t \left[\widetilde{S}_{ij} - \frac{1}{3} \widetilde{S}_{kk} \delta_{ij} \right] + \frac{2}{3} \bar{\rho} k^{sgs} \delta_{ij}, \quad (7)$$

where \widetilde{S}_{ij} denotes the resolved strain rate tensor, and δ_{ij} is the Kronecker delta. The sub-grid total enthalpy is obtained as

$$H_j^{sgs} = -\bar{\rho} \frac{\nu_t}{Pr_t} \frac{\partial \widetilde{H}}{\partial x_j}, \quad (8)$$

where \widetilde{H} is the filtered total enthalpy, and Pr_t is the turbulent Prandtl number, assumed to be unity [27]. The total enthalpy term \widetilde{H} is obtained as

$$\widetilde{H} = \widetilde{h} + \frac{1}{2} \widetilde{u}_i \widetilde{u}_i + k^{sgs}, \quad (9)$$

where \widetilde{h} is the specific enthalpy of the mixture. Following [14, 27], the sub-grid convective species flux is obtained as

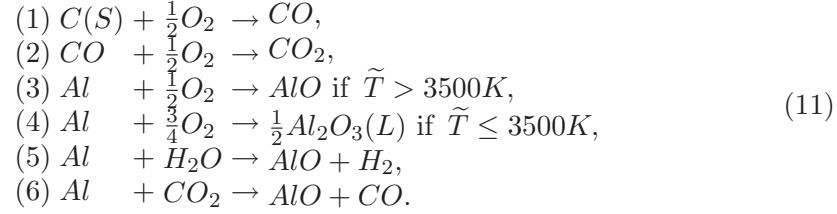
$$Y_{i,k}^{sgs} = -\frac{\bar{\rho} \nu_t}{Sc_t} \frac{\partial \widetilde{Y}_k}{\partial x_i}, \quad (10)$$

where Sc_t is the turbulent Schmidt number, assumed to be unity [27]. For the present study, the other two sub-grid terms, σ_j^{sgs} and $\theta_{i,k}^{sgs}$, are neglected; however, these terms may have to be revisited in future studies.

The terms that appear on the right side of the governing equations (Equations (1)-(4)), viz. $\widetilde{\rho}_s$, $\widetilde{F}_{s,i}$, \widetilde{Q}_s , \widetilde{W}_s and $\widetilde{S}_{s,k}$, denote the source/coupling terms due to inter-phase interaction, and are obtained from the Lagrangian tracking of the solid particles, discussed elsewhere [2].

To close chemistry, the chemical reaction rate, ω_k , is assumed to be infinitely fast, i.e., the reaction rate is dictated by turbulent mixing, rather than by kinetics/temperature (this approximation is widely referred to as the ‘‘flame-sheet’’

approximation). This approach has been used in the past for modeling the post-detonation flow-field of explosives [33], especially because an Arrhenius-type reaction rate applicable for the very high pressures and temperatures behind an explosion is not available in literature. The infinite chemistry assumption does not however account for sub-grid turbulent micro-mixing effects, which can play a role in turbulence-chemistry interactions, as well as smoothen out species gradients at micro-scales. We assume a six-step chemistry, and consider the following chemical equations (\tilde{T} : resolved gas temperature):



Aluminum combustion can be aerobic as well as anaerobic [2]. The aerobic reactions are represented by the 3rd and 4th reactions, while the anaerobic by 5th and 6th; the terms ‘aerobic’ and ‘anaerobic’ here are based on the choice of the oxidizer: O_2 or otherwise. Furthermore, we use temperature dependent curve-fits for the specific heats, $C_p(T)$ for the species [16]. Note that the species $C(S)$ and $Al_2O_3(L)$ exist in the condensed phase, and thus we use their respective condensed phase $C_p(T)$ curve-fits. For thermodynamic closure, we employ the Noble-Abel equation of state [17, 33], which is typically used for post-detonation behavior of explosives, and is given by

$$\bar{P} = \frac{\bar{\rho} R \tilde{T}}{1 - An}, \tag{12}$$

where R denotes the gas constant, n is the number of moles per unit volume, and A is an empirical constant. The term An is ~ 0.75 in the vicinity of the initial detonation wave, but rapidly transitions to zero thereafter (our experience shows that for a 5.9 cm radius TNT charge, An decreases to $O(10^{-3})$ in about 0.15 msec). Within the initial explosive charge, detonation profiles based on the Gas-Interpolated-solid Stewart-Prasad-Asay (GISPA) method [2, 3, 41, 42] are computed using the conventional one-dimensional Euler equations. Here, the pressure, density and velocity profiles are obtained from the one-dimensional GISPA method, and extrapolated to a three-dimensional sector grid (to be discussed in Section 3) in the radius corresponding to the initial explosive charge. The detonation profile within the TNT charge is obtained from the GISPA procedure can be found elsewhere [2].

The flow-field for the three-dimensional simulations involves both discontinuities such as shocks and contact surfaces, as well as relatively smoother turbulent regions; it is customary to use a numerical scheme that can handle both natures of the flow. To this end, we use a hybrid approach that uses the MUSCL (Monotone Upstream-centered Schemes for Conservation Laws) [39] shock-capturing scheme in regions dominated by discontinuities, and a central scheme in relatively smooth regions of turbulence [14]. For the shock-capturing scheme, the HLLC Riemann solver [39] is used in directions normal to the discontinuity, and the HLLC approach in the tangential directions so that the carbuncle effects can be minimized [14]. The scheme is second order accurate in both time and space. Several canonical studies have been carried out recently to verify the simulation strategy and the

numerical approach used in the current hydrocode [2, 3, 14].

2.2 Solid Phase

For the solid phase, we use the Lagrangian tracking approach to compute the particle velocity vector ($u_{p,i}$) from the forces acting on a particle, i.e., Newton's law. The particle position vector ($x_{p,i}$) is obtained from the velocity vector. These kinematic equations are summarized below for a particle in the i -th direction:

$$\frac{dx_{p,i}}{dt} = u_{p,i}, \quad (13)$$

$$m_p \frac{du_{p,i}}{dt} = \frac{\pi}{2} r_p^2 C_D \bar{\rho} |\tilde{u}_i - u_{p,i}| (\tilde{u}_i - u_{p,i}), \quad (14)$$

where m_p is the solid particle mass and r_p is the particle radius. In the above equation, C_D represents the drag coefficient and is usually expressed as an empirical function of Reynolds number (Re) [11]. Other forces on the particle such as pressure gradient, Saffman lift, Magnus effect, Basset term, etc. [12] have been neglected in the present study based on an order of magnitude estimate. We use the idea of a parcel to represent a group of particles with the same position, velocity, temperature and radius [2]. The heat transfer between the two phases is estimated assuming convection and radiation, and is used to obtain the solid particle temperature (T_p) as follows:

$$m_p C_p \frac{dT_p}{dt} = 2\pi r_p \kappa Nu (\tilde{T} - T_p) - \dot{m}_p L_v + 4\pi r_p^2 \epsilon \sigma (\tilde{T}^4 - T_p^4). \quad (15)$$

In the above equation, C_p represents the specific heat of the solid particle; κ , the thermal conductivity of the gas phase; L_v , the latent heat of vaporization; ϵ , the emissivity; and σ , the Stefan-Boltzman constant. In the literature, the Nusselt number (Nu) is typically expressed as empirical functions of Reynolds and Prandtl numbers [12]. The inter-phase mass transfer is obtained as:

$$\frac{dm_p}{dt} = -\dot{m}_p = \frac{d}{dt} \left(\frac{4}{3} \pi \rho_p r_p^3 \right), \quad (16)$$

where ρ_p denotes the particle material density. It is very critical to accurately compute the last term of the above equation, essentially $\frac{dr_p}{dt}$. To obtain this term, we employ the widely used empirical quasi-steady evaporation law following other studies [2, 6, 18]:

$$\frac{dr_p}{dt} = -\frac{r_p}{t_b} \left(1 + 0.276 \sqrt{Re} \right), \quad (17)$$

where t_b denotes the burning time; this term is critical to the accurate prediction of the evaporation rate of aluminum. As mentioned in Section 1, two regimes of aluminum combustion exist: diffusion and kinetic [4, 25, 36], and appropriate burn

times need to be used. For simplicity, we use the evaporation law as specified in Equation (17), and use the burn time data from [36]. Furthermore, we assume the ignition temperature of the aluminum particles to be 1000 K [2]. A 4th order Runge-Kutta scheme is used to solve the solid phase governing equations to obtain the solid particle position vector, velocity vector, temperature and radius.

3. Results and Discussion

The simulation hydrocode has been extensively tested with many canonical studies, and has a demonstrated record for simulating problems similar to the current undertaking [2, 3, 14]. In the present study, we consider a 5.9 cm radius TNT charge with an ambient distribution of a cloud of aluminum particles. A 45° spherical sector grid centered about the equator is used with free-slip boundary conditions along the sides of the sector, and outflow in the outermost plane; the one-dimensional GISPA detonation solution (Section 2) is extrapolated into the three-dimensional sector grid within the initial 5.9 cm radius charge (see [1] for more discussions on the sector grid approach). The initial detonation products are obtained from the balanced chemical equation: $C_7H_5N_3O_6(TNT) \rightarrow 1.5N_2 + 2.5H_2O + 3.5CO + 3.5C(S)$.

Aluminum particles of size 5 μm radius are randomly distributed in the region from outside the charge to a radial location of 8.68 cm, occupying an initial mass loading ratio (ratio of mass of solid to mass of air in a given volume), $\eta=1$. Grids of sizes $1000 \times 45 \times 45$, $1000 \times 60 \times 60$ and $1000 \times 90 \times 90$ are tried in the radial (r), azimuthal (θ) and zenith (ϕ) directions, respectively, and our experience shows that whereas the $1000 \times 45 \times 45$ grid barely suffices to resolve the mixing layer boundaries, the $1000 \times 60 \times 60$ grid is required to resolve the dispersion characteristics of the particles upon their interaction with the hydrodynamic structures in the mixing layer. Thus, for the rest of this study, we employ the $1000 \times 60 \times 60$ grid. Figure 2 presents a schematic of the initial setup showing the TNT charge, the ambient cloud of aluminum particles and air. For the aluminum combustion model, Equation (17), we use the burn time, t_b , based on recent experimental data [36], which conforms to the kinetic regime of aluminum burning. Focus here, *inter alia*, is on particle ignition, combustion, clustering and dispersion.

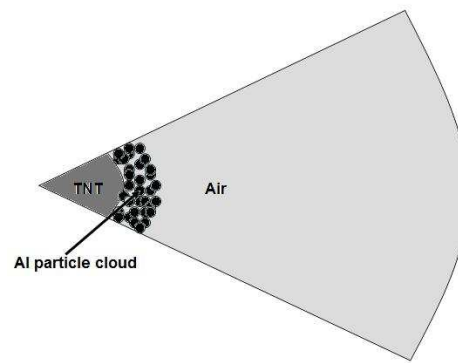


Figure 2. Initial setup used for the simulations (charge and particle sizes not to scale). Note: this is a schematic only.

We normalize all times presented in the rest of the paper using the time required for the detonation completion within the charge, t_o . For comparisons, explosives are generally scaled using $W^{1/3}$, where W represents the mass of the explosive in the initial charge [1]. Since $W \sim r_o^3$, where r_o denotes the initial charge radius,

Table 1. Summary of the different cases considered in this study

Case	r_p in μm	η	Radial cloud width in cm	Remarks
1	5	1	5.9-8.68	baseline case
2	5	2	5.9-8.68	effect of η
3	10	1	5.9-8.68	effect of r_p
4	10	1	5.9-12	effect of radial cloud extent
5	5	1	5.9-8.68	afterburn turned off
6	5	1	5.9-8.68	different choice of t_b ($t_b = 1$ msec)
7	5	1	5.9-8.68	different choice of t_b ($t_b = 0.4$ msec)

and $t_o = r_o/D$, where D represents the detonation velocity of the explosive used, the choice of using t_o to scale times is equivalent to the use of $W^{1/3}$. For a 5.9 cm radius TNT charge, the GISPA simulation (described in Section 2) predicts $t_o = 8.25 \mu\text{sec}$, and we use this scaling for the times reported in the rest of the paper.

The simulation case with $r_p = 5 \mu\text{m}$, $\eta = 1$ and the initial cloud extending from outside the charge ($r = 5.9$ cm) till $r = 8.68$ cm is chosen as the baseline case for the analysis to explain the primary physics. Parametric studies will follow this analysis with the consideration of other particle sizes, loading ratios, initial radial extent of the particle cloud, and the choice of the aluminum evaporation burn time (t_b in Equation (17)). A summary of the different cases considered in this paper is presented in Table 1.

3.1 Dispersion and Ignition

The primary physics of the post-detonation phase of the baseline case (Case 1 in Table 1) as observed from our simulation is summarized here. As mentioned in Section 1, when the detonation wave reaches the outer boundary of the initial charge, a primary shock wave (PS) propagates outwards and a rarefaction wave inwards. The contact surface initially overtakes the particles, and due to the high density gradients across it, is sensitive to perturbations. The particles pick up momentum and heat from the gas, and thereby introduce perturbations on the contact surface. These perturbations subsequently grow into Rayleigh-Taylor [38] hydrodynamic instabilities at multiple transverse scales and wavelengths. By $t/t_o \sim 4$, the entire particle cloud is engulfed into the detonation products. At the same time, the inward moving rarefaction overexpands the local flow, giving rise to a secondary shock (SS) [7]. This SS is initially a weak compression wave and is swept outwards by the outward expanding gases, during which it strengthens. The schematic of the post-detonation flow-field presented earlier in Figure 1 is based on this simulation case. However, note that this representation in Figure 1 is in a one-dimensional sense only; in reality, the contact surface will develop into a three-dimensional mixing layer (also termed as a fire-ball).

Ignition occurs in the cloud around $t/t_o \sim 5$, initially at the leading edge by virtue of it being closer to the source of heat—that due to the afterburn between the inner detonation products and the outer air. Subsequently, the hydrodynamic structures decelerate more than the particles, as the latter have a higher inertia; this results in the leading edge of the particle cloud to catch-up and interact with the structures—the second interaction. Around this time instant, while the leading edge (LE) of the particle cloud is in the mixing layer where the detonation products ($C(S)$, CO , H_2O), air, and afterburn products (CO , CO_2) co-exist, the trailing edge (TE) of the cloud is still engulfed into the detonation products. Furthermore, around this time instant ($t/t_o \sim 5$), the SS, which is still a compression wave,

penetrates into the TE of the cloud, and subsequently strengthens into a shock around $t/t_o \sim 8$; note that this strengthening is not due to the particles, but due to coalescence of pressure pulses arising from the relatively higher pressure immediately behind the PS (see [7] for more discussions on the formation of the SS). Following this, the SS slows down faster than the particles, as the latter has a higher inertia. By $t/t_o \sim 12$, the particles are completely engulfed between the PS and SS, and interact with the Rayleigh-Taylor structures that have already started to grow; this growth of the structures in size is due to two reasons: (1) entrainment of the outer air into the structures; and (2) “bubble competition” between contiguous structures [2, 23, 28, 29]. Note that this second interaction between the particle cloud and the contact surface (which by now is essentially a highly perturbed surface due to the growth of the Rayleigh-Taylor structures) lasts for a longer time than their first interaction, as the hydrodynamic structures have grown to a larger transverse scale and width by this time.

Around $t/t_o \sim 35$, the SS implodes inwards as the pressure has reduced considerably near the core due to the earlier rarefaction wave. During this implosion phase, the TE of the particle cloud slows down as the local gas velocity reverses—this inevitably widens the particle cloud width. At the same time, the LE of the cloud starts to emerge out of the hydrodynamic structures, whose growth hitherto has ensued in a mixing layer. At this time, the choice of the oxidizer varies across the width of the particle cloud for the aluminum combustion—it is O_2 near the leading edge (aerobic); is H_2O near the TE (anaerobic), and a mixture of possible oxidizers (CO_2, H_2O, O_2) in the middle of the cloud that is currently in the mixing layer. Furthermore, by this time ($t/t_o \sim 35$), about 75% of the initial aluminum by mass has already evaporated, indicating that most of aluminum evaporation occurs primarily when the particles are engulfed inside the detonation products.

Vortex rings exist around the hydrodynamic structures [21] due to shear and baroclinic effects, and they introduce transverse velocity components to the otherwise radially dispersing particle cloud. This transverse dispersion of the particles leads to their clustering (preferential accumulation) around these vortex rings. Thus, a “foot print” of the Rayleigh-Taylor structures is left on the particle cloud and is preserved even until much later—we will soon revisit this phenomenon. Note that we refer to particle structures as a ‘cluster’, merely to distinguish it from hydrodynamic structures; thus, for the remainder of this paper, we refer to hydrodynamic fluid structures simply as ‘structures’, and particle structures as ‘clusters’ to avoid confusion.

Subsequently, beyond $t/t_o \sim 75$, the particle cloud leaves the mixing layer, and is quenched shortly thereafter due to the unavailability of heat and the relatively cooler surrounding air; analysis shows that only 12% of the original aluminum mass remains un-evaporated in the solid phase for the chosen particle radius ($r_p = 5 \mu\text{m}$) and mass loading ($\eta=1$). Furthermore, outside the mixing layer, the sources of turbulence and vorticity are not as preponderant as in the mixing layer; thus, the particles disperse mostly along the radial direction once outside the mixing layer, maintaining their clustered shape, i.e., the earlier hydrodynamic-induced foot print in the cloud is maintained. Aerodynamic drag slows down the particles and their clustered shape grows in size as they expand outwards into free space. Meanwhile, the SS that has been imploding, reflects from the origin ($t/t_o \sim 125$), and subsequently explodes outwards. During this second outward passage, the SS interacts with the hydrodynamic structures in the mixing layer—giving rise to a Richtmyer-Meshkov instability [32]—this event is also termed as a ‘reshock’ [1, 20]. Here, the pressure gradient across the secondary shock is mis-aligned with the density gradients across the hydrodynamic structures, which results in the creation

of vorticity due to baroclinic torque effects ($\dot{\omega} = \frac{1}{\rho^2} \nabla p \times \nabla \rho$). This vorticity sustains afterburn, as it allows for fresh sources of oxygen in the air that was hitherto unreachable to the inner detonation products, to come into contact. Furthermore, during this reshock the mixing layer is compressed [1, 20], due to which the vorticity is able to sustain itself for a slightly longer time, a consequence of the two stretching terms in the vorticity equation [2]. Subsequently, around $t/t_o \sim 325$, the SS catches-up with the particle cloud and penetrates it, essentially a reshock for the particle cloud, thereby shrinking the width of the cloud. However, the quenched particles do not re-ignite, as their interaction with the SS occurs radially far away, and the latter has already attenuated due to spherical spreading. To illustrate the aforementioned hydrodynamic instabilities behind the blast wave, we present the isosurface of the mass fraction of CO , shaded with $\ln(\rho)$ in Figure 3 at times (a) $t/t_o \sim 35$ and (b) $t/t_o \sim 460$. As evident, at the earlier time, the hydrodynamic structures are spatially organized and are mushroom shaped; at the later time, which is after the reshock, the structures are more convoluted/wrinkled owing to the deposited vorticity.

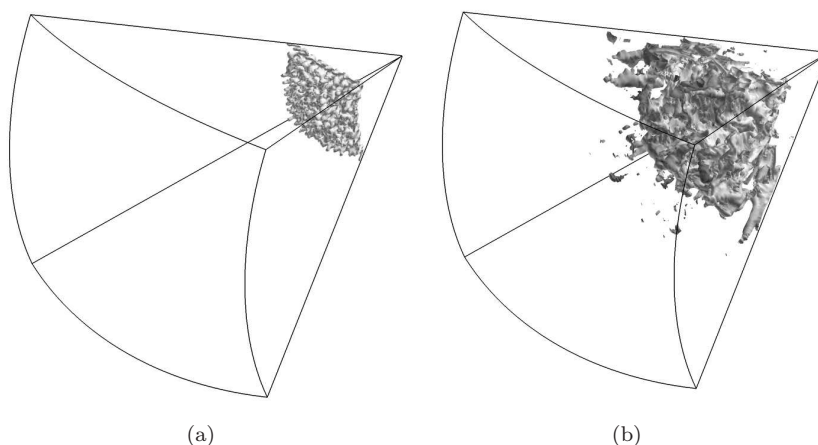


Figure 3. CO isosurface shaded with $\ln(\rho)$ at times (a) $t/t_o \sim 35$; (b) $t/t_o \sim 460$. Particles are not shown for better clarity.

3.2 Chronology of Particle Clustering

Here, we further elaborate on the physics of particle clustering effects. The clustering of solid particles due to isotropic turbulence is well known [35]; however, here the clustering is owing to the interaction of the particle cloud with the hydrodynamic structures. One main difference is that in isotropic turbulence, the vortices have no directional bias; consequently, no spatial bias for the particle clusters. However, in the present problem, the vortex rings exist only around the Rayleigh-Taylor structures which are spatially aligned along the radial direction. Hence, the clustering shapes of the particles due to explosion are also spatially biased. We have also verified that clustering of particles occurs even when the sub-grid turbulence model is turned off, i.e., the clustering is not a consequence of the sub-grid modeling aspects, but is physical.

Vorticity in the mixing layer is primarily concentrated around the Rayleigh-Taylor structures, i.e., at the interface between the two fluids, due to shear and baroclinic effects. In regions between contiguous structures where the fluid is air only, and in the regions inside the structures where the fluid is only the detonation

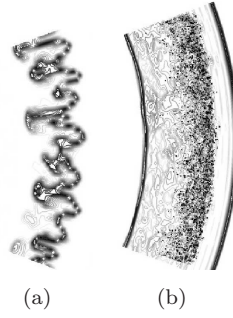


Figure 4. Interaction of the particle cloud with the hydrodynamic structures at $t/t_o \sim 35$: (a) CO_2 mass fraction; (b) $\ln(\omega)$ contours and particle locations.

products, vorticity is not as significant. This gives rise to local regions with vorticity (at the tip of the hydrodynamic structures), and those without significant flow rotationality (regions between contiguous structures and inside the structures). To better illustrate the clustering phenomena, the CO_2 mass fraction and vorticity (ω) contours are presented in Figure 4, along with the particles (shown as black dots) at $t/t_o \sim 35$ —one of the time instants corresponding to the interaction of the particle cloud with the hydrodynamic structures; these profiles are zoomed near the interaction region and presented. The outer and inner bold lines in Figure 4 (b) represent the primary and secondary shocks, respectively. Vorticity is accumulated near the product regions, and particles interact with this vorticity, causing them to cluster. The particle cloud is virtually unaffected in the vorticity-free regions, but is inevitably influenced in the regions dominated by the vortices; this, essentially, gives rise to the preferential accumulation (or concentration) of particles.

The clustering patterns of the particle cloud is now discussed, and is presented chronologically in Figure 5 (the view presented is that as seen from the outermost plane of the sector looking inwards at the origin). At early times (Figure 5 (a)), the expanding particle cloud is still completely engulfed into the detonation products, and no clustering effects are evident due to the absence of vorticity. Subsequently, the particles enter the mixing layer; since they enter the mixing layer from the inside, the particles first encounter the vortex rings around the bubbles (Figure 5 (b)). The vorticity around these rings causes the particles to also disperse in the transverse directions, and this centrifugal (θ and ϕ directions) motion combined with their inertia, results in the particles to cluster around the vortex rings (more discussions below). Essentially, the transverse dispersion causes the particles to be flung out from the core of the vortex rings of the hydrodynamic structures [10]. Later, the dispersion is complete, and the particles are clustered by $t/t_o \sim 50$ (Figure 5 (d)). Furthermore, the particle cloud front is also corrugated due to the local dispersion of the particles due to the vorticity in the hydrodynamic structures during the interaction event; note that this interaction event is not instantaneous, but lasts for a finite, albeit small period of time (from $t/t_o \sim 20$ till $t/t_o \sim 60$). After this, the particles leave the mixing layer, and enter vortex-free regions, thereby preserving their clustered shape, i.e., the hydrodynamic ‘foot print’ (Figure 5 (e)). Note that beyond $t/t_o \sim 50$, even though the clustered cloud shape is preserved (albeit not size), the particles are still moving in the radial direction as the frontal surface area of the cloud increases. Thus, even outside the mixing layer the physical size of the clusters increases with time due to the radial-only dispersion of the particles, but the angular size and the shape of the clusters are frozen. We have appropriately adjusted the different sub-figures presented in Figure 5 for better clarity of illustrating the transverse motion only.

The dispersion characteristics of particles and the formation of clusters when

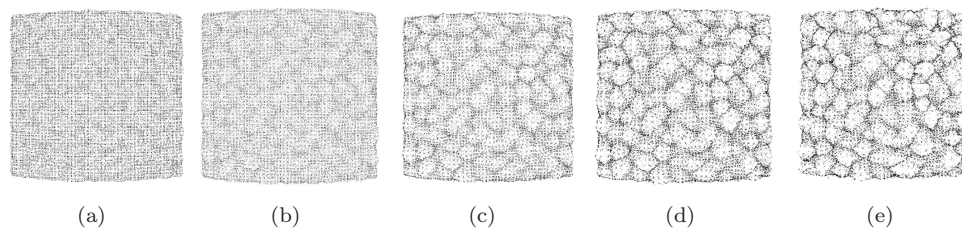


Figure 5. Clustering of particle cloud at times t/t_o (a) 20; (b) 25; (c) 35; (d) 50; (e) 560. The scales of the figures have been adjusted for better clarity.

particle clouds interact with fluid structures is dictated by the Stokes number, St , which is the ratio of the particle's momentum response time to the flow field time scale, and is given by the expression

$$St = \frac{\rho_p d_p^2 / 18\mu}{L_o / U_o}, \quad (18)$$

where ρ_p is the particle material density, d_p is the particle diameter, μ is the viscosity of the gas, and L_o and U_o denote, respectively, the flow length and velocity scales. In previous studies, different dispersion characteristics for different St have been reported [9, 10, 24]. While particles with very small St tend to follow the flow, particles with St of the order of unity tend to accumulate near the circumference of fluid structures [24]. Particles with slightly larger St , on the other hand, tend to accumulate near the regions of low vorticity and high strain [24]. The clustering patterns observed in Figure 5 are reminiscent of those presented in [24] (see for instance Figure 19 of this ref.), where the authors study the particle dispersion characteristics in a three-dimensional temporal mixing layer using direct numerical simulations. In the current study, analysis shows St of the order of unity for the $r_p=5 \mu\text{m}$ particles (which are $r_p=2.5\text{--}3 \mu\text{m}$ during their interaction with the Rayleigh-Taylor structures); and St of the order of 10 for $r_p=10 \mu\text{m}$ particles (which are $r_p=8\text{--}8.5 \mu\text{m}$ during their interaction with the Rayleigh-Taylor structures). Furthermore, the particles are also travelling at speeds in excess of 1 Km/s in the radial direction, and so the time they have to interact with the hydrodynamic structures is limited, indicating that in addition to the particle response time scale, the residence time—time a particle takes to traverse the hydrodynamic structures—is also of significance. Note that the transverse velocity component is used for the definition of U_o and not the radial velocity, since the focus here is on clustering of particles due to transverse motion.

3.3 Parameters that Affect Particle Clustering

3.3.1 Particle mass loading ratio

To investigate the effect of mass loading ratio, we also consider $\eta=2$ for the same particle radius ($5 \mu\text{m}$) and initial radial extent of the particle cloud distribution (radial location 5.9–8.68 cm), i.e., Case 2 in Table 1. Recently, we observed more mixing in the gaseous detonation products when the initial particle loading ratio is higher [2]; specifically, the mixing layer width is wider and, consequently, more of the detonation product fuel was consumed, i.e., more afterburn when the initial outer particle cloud mass loading ratio is higher. Note that this enhanced mixing is due to more perturbations introduced to the contact surface during the first interaction

event between the particles and the contact surface. These enhanced perturbations later result in stronger/larger vortex rings around the Rayleigh-Taylor structures for the $\eta=2$ case than for $\eta=1$. Consequently, the interaction of the particle cloud with these structures, i.e., the second interaction, is also more prominent when the initial particle loading ratio is higher.

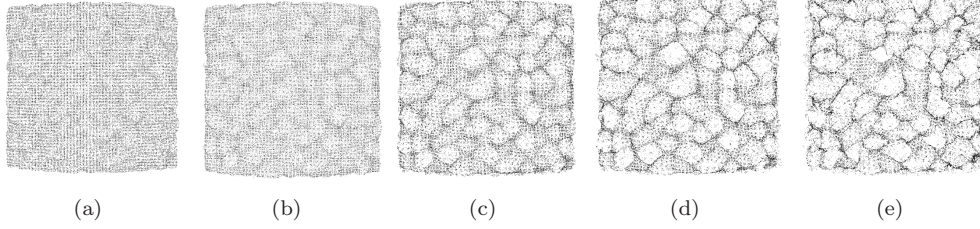


Figure 6. Effect of η on clustering of particle cloud ($\eta=2$): times t/t_o (a) 20; (b) 25; (c) 35; (d) 50; (e) 560. The scales of the figures have been adjusted for better clarity.

The clustering process is chronologically presented in Figure 6 for $\eta=2$; closer observation reveals that due to this larger vortex rings for $\eta=2$, many clusters, albeit not all, appear larger due to more dispersion for $\eta=2$ —a direct consequence of the stronger vortex rings in the ensuing Rayleigh-Taylor structures. Moreover, some clusters in Figure 6 appear as a combination of two partial clusters. This formation is owing to the particle cloud having earlier interacted with two merging hydrodynamic structures; recall from Section 1, the bubble competition process prevalent in the mixing layer that can result in contiguous hydrodynamic structures to interact. Thus, when the particle cloud interacts with two competing hydrodynamic structures, it disperses locally corresponding to this ‘merging shape’, and this shape is preserved even at later times (Figure 6 (e)). Since $\eta=2$ (Figure 6) results in more merging shapes of the particle cloud than $\eta=1$ (Figure 5), we believe that bubble competition is more significant for $\eta=2$ —due to more perturbations introduced to the contact surface during the first interaction event by the higher loading particle cloud.

For a better understanding of the actual clustering process, it is of interest to track the local transverse gas velocities as ‘seen’ by different particles as they disperse. To this end, we consider four groups of particles based on their initial locations in the cloud, and denote as $C60$, a collection of 100 randomly chosen particles initially located at radial location $r = (6.0 \pm 0.1)$ cm; as $C70$, a collection of 100 randomly chosen particles initially located at radial location $r = (7.0 \pm 0.1)$ cm; similarly, $C80$ corresponding to $r = (8.0 \pm 0.1)$ cm; and $C86$ corresponding to $r = (8.6 \pm 0.1)$ cm. Of particular interest here is the average local gas velocity as ‘seen’ by the particles corresponding to each group. Note that for the averaging, we consider absolute values, i.e., $|u_{gas,\theta}|$ & $|u_{gas,\phi}|$, so that two particles at diametrically opposite ends of a vortex ring, which ‘see’ local gas velocities equal in magnitude, but opposite in direction, do not cancel out in the averaging.

For the cases corresponding to $r_p=5$ μm , initial cloud extending radially from $r=5.9$ – 8.68 cm, and $\eta=1$ & 2 , Figure 7 presents the average local gas velocity as seen by the particles corresponding to the groups $C70$ (Figure 7 (a)) and $C86$ (Figure 7 (b)) (similar results also hold for $C60$ and $C80$, not shown here for brevity). At very early times, the local azimuthal ($u_{gas,\theta}$) and zenith ($u_{gas,\phi}$) velocity components are almost negligible, but rise up fast as the particles pick up momentum from the gas and are set into motion. Around $t/t_o \sim 20$, the particles start to interact with the vortex rings around the hydrodynamic structures, as evident from the peaks in Figures 7 (a) & (b). Around $t/t_o \sim 30$, the transverse local gas velocities

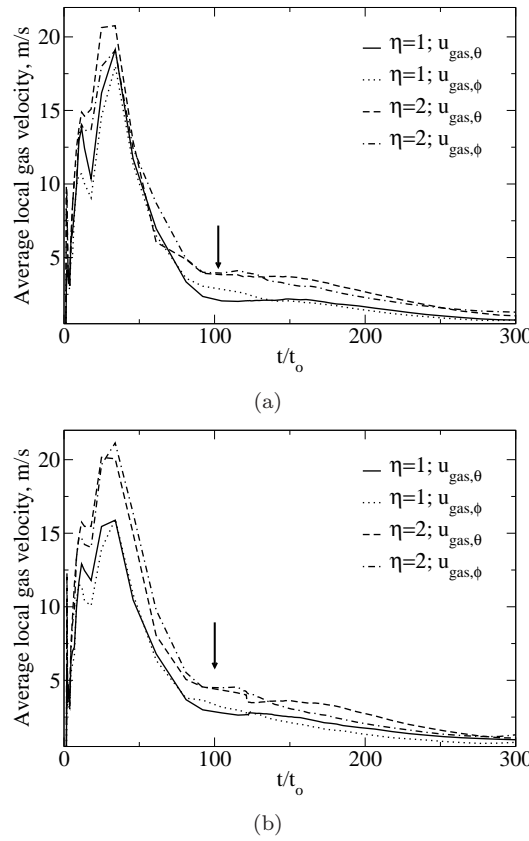


Figure 7. Effect of η on the average local gas velocity seen by the particles for particle group (a) C70; (b) C86.

are ~ 20 m/s—this creates significant enough transverse velocities that clusters the particles around the hydrodynamic structures. Comparing the two different η cases, as evident from Figure 7, the local average gas transverse velocity components are slightly higher for the $\eta=2$ case during the peak of the second interaction ($t/t_o \sim 30$). Subsequently, the average local azimuthal and zenith gas velocities as seen by the particles are also higher, by a factor of $1.5 - 2$ near the region indicated by the arrow. This sustained higher transverse velocities in the gas for $\eta=2$ results in the slightly more pronounced clustering observed for the higher loading ratio in Figure 6.

3.3.2 Particle size and distribution

Recently [2], we observed particles larger than about $20 \mu\text{m}$ radius not to be susceptible to the formation of clusters for the chosen explosive conditions (initial charge size, explosive used: TNT, particle mass loading ratio, initial cloud width, etc.). In [2], we concluded that the mixing and afterburn aspects in the gas phase are nearly independent of particle size for the same initial mass loading ratio (η) and initial radial extent of the particle cloud. Furthermore, we also showed in [2] that more mixing occurs when the initial cloud distribution extends farther. Here, we compare the clustering effects due to $5 \mu\text{m}$ and $10 \mu\text{m}$ particle radius, for $\eta=1$, and initial radial extent of the cloud $r=5.9\text{--}8.68$ cm (Cases 1 & 3 in Table 1). Our analysis shows that the $10 \mu\text{m}$ radius particles do not form clusters for the chosen conditions, as their ignition is delayed *vis-à-vis* the $5 \mu\text{m}$ radius particles, due to which the particles are still sufficiently large ($\sim 8\text{--}8.5 \mu\text{m}$ radius) during the second interaction event with the hydrodynamic structures. On the other hand, the particles in the $5 \mu\text{m}$ cloud have already ignited during their engulfment into

the detonation products, and are about $2.5\text{--}3\ \mu\text{m}$ in radius during the second interaction event. The inter-phase momentum transfer time scales as r_p^2 , where r_p denotes the particle radius; i.e., larger particles take longer to be influenced by the flow. Hence, the particles corresponding to the $10\ \mu\text{m}$ cloud, by virtue of their higher inertia during the second interaction event, are not easily dispersed by the hydrodynamic vortex rings. Consequently, the $10\ \mu\text{m}$ particle cloud does not form clusters upon their explosive dispersal for the chosen conditions ($\eta=1$; initial cloud width = $5.9\text{--}8.68\ \text{cm}$, etc.). Due to this subdued dispersion of the cloud, even the width of the $10\ \mu\text{m}$ particle cloud is nearly preserved with time, not shown for brevity.

By considering $10\ \mu\text{m}$ radius particle clouds of the same mass loading ratio ($\eta=1$), but an initial distribution extending from radial location $r=5.9\text{--}12\ \text{cm}$ (Case 4 in Table 1), significant differences are observed; in Figure 8, we present the particle cloud at different times for this case. Comparing this with the aforementioned case with the $5\ \mu\text{m}$ radius particles (Figure 5), it is evident that although clusters form for the $10\ \mu\text{m}$ radius particle cloud when initially distributed from $r=5.9\text{--}12\ \text{cm}$, they are much fewer in number and are not prominently visible, i.e., they are more or less degenerate clusters. Furthermore, the clusters are relatively ‘diffuse’ in the sense that the regions of higher particle concentration only gradually change to regions of lower concentration *vis-à-vis* the sharp particle concentration gradients observed for the $5\ \mu\text{m}$ particle radius (Figure 5). Thus, although more particles (and more mass) are now present for the $10\ \mu\text{m}$ cloud extending initially from 5.9 to $12\ \text{cm}$ than the $5\ \mu\text{m}$ cloud extending initially from 5.9 to $8.68\ \text{cm}$, both corresponding to $\eta=1$, the particle clustering effect is more significant for the latter, due to the shorter momentum transfer time scales during their interaction with the hydrodynamic structures. Hence, the particle size during the second interaction event is critical to the cluster formation.

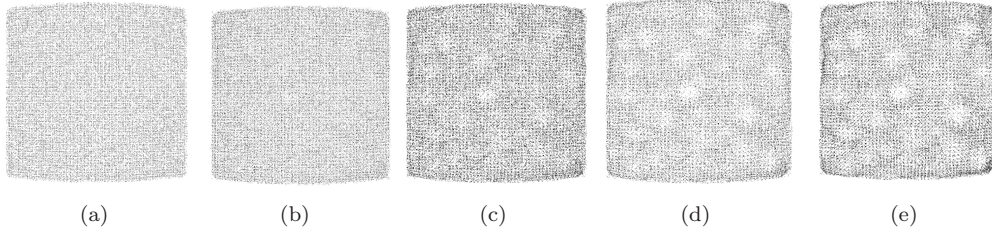


Figure 8. Effect of particle size on clustering of particle cloud ($r_p=10\ \mu\text{m}$; initial cloud distribution: $5.9\text{--}12\ \text{cm}$; $\eta=1$): times t/t_o (a) 20; (b) 25; (c) 35; (d) 50; (e) 560. The scales of the figures have been adjusted for better clarity.

To illustrate the effect of the local gas velocity in support of the observations made in Figure 8, we present the average local gas azimuthal ($u_{gas,\theta}$) and zenith ($u_{gas,\phi}$) velocities as seen by the particle groups *C70* and *C86* in Figure 9 for $r_p=10\ \mu\text{m}$, $\eta=1$, and the initial particle cloud extending radially from (1) $r=5.9\text{--}8.68\ \text{cm}$ and (2) $r=5.9\text{--}12\ \text{cm}$ (the definitions of *C70* and *C86* are the same as described previously). As evident from Figure 9, the average local azimuthal and zenith gas velocities as seen by the particles are higher, when the initial cloud width is wider and, consequently, the clustering is more pronounced. More particles are available to perturb the flow, and the total perturbation time on the contact surface by the particles during the first interaction event is longer for a wider initial cloud width; hence, significantly higher transverse velocities are seen by the particles as they disperse outwards. These differences in the local gas transverse velocities result in the clustering observed for $r_p=10\ \mu\text{m}$ when the particles initially extend radially

till 12 cm (Figure 8), but no clustering is observed when initially extending till 8.68 cm. We could not verify this result for $r_p=5\text{ }\mu\text{m}$ extending till 12 cm, as this setup requires too many particles to be tracked, stretching available computational memory.

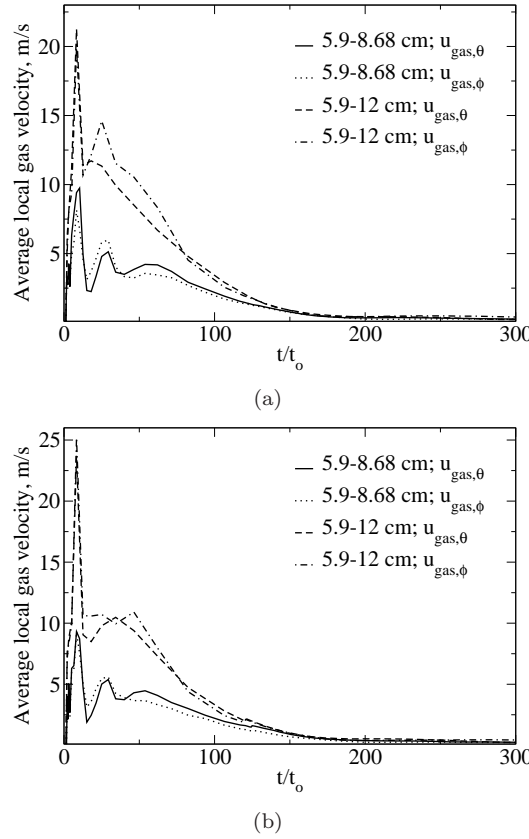


Figure 9. Effect of initial cloud width on the average local gas velocity seen by the particles for particle group (a) C70; (b) C86.

3.4 Mixing Layer Boundaries and Width

Also of interest is the quantification of the dynamics of the mixing layer, so as to shed light on the mixing process between the inner detonation products and the outer air. To this end, we first define the mixing layer (*ML*) boundaries based on the mass fraction of *CO*, as also done in our recent study [2]. Four phases are of interest here for the gas: (a) blast wave; (b) implosion; (c) reshock; and (d) asymptotic mixing [1, 2, 20, 21] (these references describe the four phases more elaborately). The inner and outer boundaries of the *ML* are presented in Figure 10 (a) for the 5 and 10 μm particle radius cases, corresponding to $\eta=1$, and the initial cloud extending from $r=5.9$ -8.68 cm. The afterburn energy release can also play a central role in the dynamics of the *ML* as this inevitably results in volumetric expansion of the gas in the *ML*; to investigate its significance, we also consider a case with 5 μm particle radius, but with the afterburn (of both the detonation products as well as the evaporated aluminum) fictitiously turned off—we refer to this case simply as ‘no afterburn’ (Case 5 in Table 1). As evident from Figure 10 (a), the implosion phase ($t/t_o \sim 125$) is delayed by about $t/t_o \sim 50$ with the afterburn turned off. Furthermore, the inner and outer boundaries stretch farther outwards without this afterburn during the implosion phase: the

outer boundary due to absence of CO consumption; the inner boundary due to a weaker secondary shock—a consequence of unavailability of the excess energy. In addition, the weaker secondary shock also results in a subdued reshock phase ($t/t_o \sim 300$ in Figure 10 (a)) for the no afterburn case in terms of the distance traversed by the lower boundary of the ML around this time (it traverses from $r/r_o = 5$ to $r/r_o = 9$ with the afterburn energy release on; $r/r_o = 7$ to $r/r_o = 8$, otherwise). At sufficiently late times ($t/t_o \sim 500$), the outer boundary stretches farther outside for the realistic cases than the no afterburn case, for the same reason. Thus, the afterburn exothermic energy release plays a critical role in the dynamics of the ML .

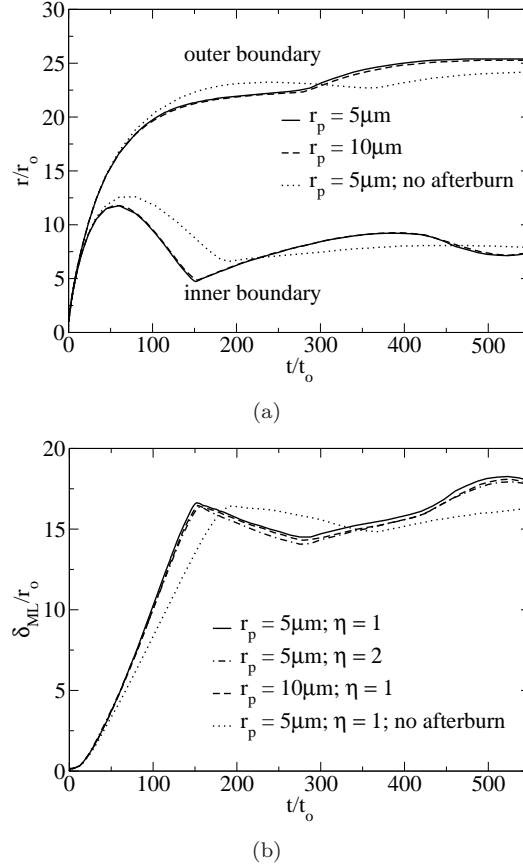


Figure 10. Growth of the mixing layer: (a) outer and inner boundaries of the mixing layer; (b) mixing layer width (δ_{ML}). Both variables are normalized with the initial charge radius, r_o .

In Figure 10 (b), we present the ML width (δ_{ML}), normalized with the charge radius, r_o , with the initial cloud extending from $r=5.9$ - 8.68 cm. Here, δ_{ML} is the spatial difference between the outer and inner boundaries of the ML . As evident, δ_{ML} grows slower during the implosion ($t/t_o \sim 125$) without the afterburn energy, due to the delayed and subdued implosion phase (Figure 10 (a)). During the asymptotic phase ($t/t_o \sim 500$), clearly the afterburning energy release expands the gases in the ML radially further, i.e., the fireball is bigger with the excess energy release, exemplifying the role played by volumetric expansion of the gas in the ML .

3.5 Particle Cloud Boundaries and Width

An investigation of the boundaries and the width of the particle cloud as it disperses is of interest to understand the exact dispersion process subsequent to the

detonation. Since the particle cloud leading (LE) and trailing edges (TE) are corrugated due to clustering effects, it is essential to define the LE and TE of the cloud to investigate their dispersion process. Here, we define the LE ($r_{98\%}$) and TE ($r_{2\%}$) of the particle cloud as the radial location corresponding to which 98% and 2%, respectively, of the total number of particles are contained. Note that this definition is rather *ad hoc*, and is used only to illustrate the dispersion process. We define the particle cloud width, $\delta_{cloud} = r_{98\%} - r_{2\%}$.

In Figure 11 (a), the LE and TE of the cloud are presented for the $5\ \mu\text{m}$ particle radius clouds considered hitherto, normalized with the initial charge radius (r_o). Also shown here are the results corresponding to $t_b=1\ \text{msec}$ (Case 6 in Table 1), which is close to recent shock tube data [26] for a similar particle size, and with $t_b=0.4\ \text{msec}$ (Case 7 in Table 1), which would be the burn time predicted with the classical d^2 law [18] for $r_p=5\ \mu\text{m}$ aluminum particles. We have identified five discernable phases of interest in the particle dispersion process: (1) engulfment phase; (2) hydrodynamic instability-interaction phase; (3) first vortex-free dispersion phase; (4) reshock phase; and (5) second vortex-free dispersion phase. As aforementioned, at early times, the particles are engulfed into the detonation products—we refer to this as the “engulfment phase.” Subsequently, the particles are readily set into motion, and interact with the hydrodynamic instabilities/structures in the *ML*—we refer to this phase as the “hydrodynamic instability-interaction phase”; note that this second phase could essentially be also referred to as the “mixing layer phase,” as the particles traverse the *ML* during this time interval. This is the phase where the clustering of particles occurs, owing to the presence of vortex rings in the hydrodynamic instabilities in the *ML*. Then, the particles leave the *ML* and penetrate into the vortex-free outer region of air. Here, the momentum picked up earlier drives the dispersion and, later the particles slow down; the dispersion during this phase is essentially radial, i.e., free of any significant three-dimensional phenomena like hydrodynamic instabilities, vortices, etc.—hence the name “first vortex-free dispersion phase.” This third phase lasts for a longer time than the earlier two phases. Subsequently, the secondary shock (SS) penetrates into the particle cloud, compressing it from the inside, as evident from the slight outward acceleration of the TE around $t/t_o \sim 325$. We refer to this phase as the “reshock phase”—not to be confused with the reshock phase pertinent to the gas as well. Our observations show that since the reshock phase for the particles occurs outside the *ML*, baroclinic effects are not significant for the particle reshock phase—note that this is not true for the gas reshock phase. Lastly, after the SS leaves the particle cloud, the LE and TE further disperse radially outwards, preserving their cluster ‘foot print’—we refer to this as the “second vortex-free dispersion phase.”

In Figure 11 (b), the cloud width (δ_{cloud}), normalized with the initial charge radius (r_o), is plotted with time, demonstrating the five different phases; we present three cases based on η and t_b , self-explanatory by the legend in Figure 11 (b). As evident, the cloud width grows faster during the hydrodynamic instability-interaction phase *vis-à-vis* the first vortex-free dispersion phase. During the particle reshock phase, δ_{cloud} decreases by about $\frac{1}{2}r_o$ and, subsequently, continues to slowly grow during the second vortex-free dispersion phase, owing to the LE being slightly faster than the TE. Also evident from Figure 11 (b) is the near-similarity of δ_{cloud} for $\eta=1$ with different t_b , showing independence to the choice of the three different burn times (t_b) used. For $\eta=2$, δ_{cloud} is about $\frac{1}{2}r_o$ greater than for $\eta=1$, and the differences between the two different η s starts to occur even at early times, showing that the concomitant enhanced mixing for a higher η leads to a wider cloud. Hence, the strength of the vortex rings during the hydrodynamic instability-interaction phase plays a critical role in the later time cloud width. Furthermore, starting

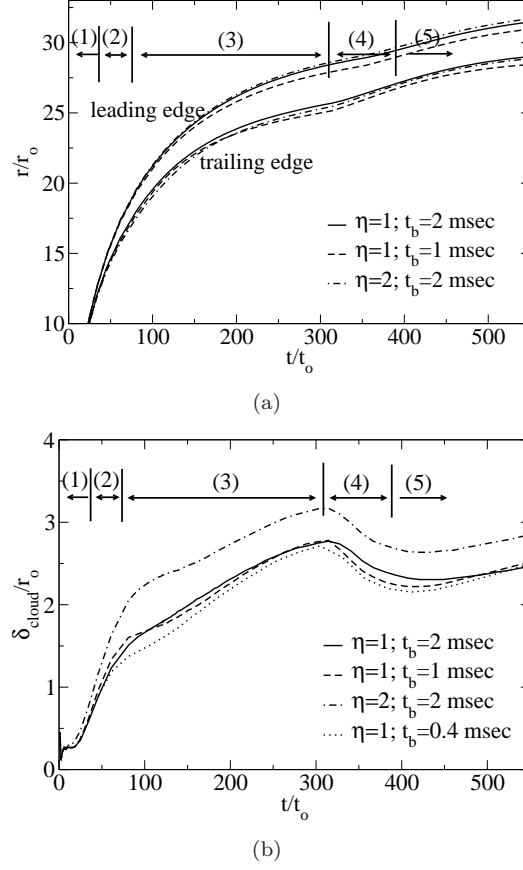


Figure 11. Different phases in the dispersion of the particle cloud: (a) leading and trailing edges of the particle cloud; (b) cloud width. The phases are denoted by (1) engulfment phase; (2) hydrodynamic instability-interaction phase; (3) first vortex-free dispersion phase; (4) reshock phase; and (5) second vortex-free dispersion phase. The particle cloud boundaries for $t_b=0.4$ msec are not presented in (a) for better clarity of the different cases shown.

from the first vortex-free dispersion phase and thereafter, δ_{cloud} for the different η s maintains a more or less uniform difference ($\sim \frac{1}{2}r_o$), showing self-similar behavior.

3.6 Scaling Laws

Scaling laws are widely used to model explosives—see the introduction section in [1]. They have also been used to model explosive ML boundaries obtained from computational simulations [1, 20]. Of interest is the variation of the ML width with time, so that the hydrodynamic growth rate of the Rayleigh-Taylor structures can be compared for different parametric test cases. Scaling laws for particle cloud dispersion can also be useful for comparing the cloud dispersion behavior. Stated in these terms, we now focus on scaling laws for the width of the ML of the explosive fireball, as well as that of the particle cloud (δ_{cloud}). Specifically, we consider the ML width (δ_{ML}) for the early blast wave and implosion phases. For the particle phases, we scale δ_{cloud} for the hydrodynamic instability-interaction and the first vortex-free dispersion phases. These are modeled using power law curve fits as $\delta_{ML}/r_o = a_{ML} t^m$ and $\delta_{cloud}/r_o = a_{cloud} t^n$, respectively, where r_o denotes the initial charge radius. The coefficients obtained from the power law curve fits are summarized in Table 1 (t in msec).

As evident from the Table, the hydrodynamic structures in the ML grow close to linear ($m \sim 1.17$) during the initial blast wave phase. Earlier studies [1, 20] have demonstrated linearity during the early blast wave phase, albeit for single-phase

Table 2. Scaling laws for the mixing layer (δ_{ML}/r_o) and particle cloud (δ_{cloud}/r_o) widths.

η	Phase	a_{ML}	m	a_{cloud}	n
1	blast wave	6.31	1.172		
	implosion	13.07	1.346		
	hydrodynamic instability-interaction			3.315	1.395
	first vortex-free dispersion			1.799	0.487
2	blast wave	6.552	1.171		
	implosion	12.743	1.315		
	hydrodynamic instability-interaction			3.687	1.259
	first vortex-free dispersion			2.33	0.326

explosive charges with an initial perturbation added near the outer periphery of the charge. We believe the slight departure from linearity for the current scenario is owing to the continuous nature of the perturbation, i.e., the finite albeit small time span of early interaction of the contact surface with the particle cloud. Thereafter, the growth becomes non-linear ($m \sim 1.31 - 1.35$) during the implosion phase, as the inner boundary of the ML is dragged inwards by the imploding secondary shock. For the particle cloud, the power law index (n) shows a slightly more pronounced dependence on the mass loading ratio (η). Whereas the index $n \sim 1.4$ for $\eta=1$, it is ~ 1.26 for $\eta=2$ during the hydrodynamic instability-interaction phase. Subsequently, during the first vortex-free dispersion phase, the index $n \sim 0.49$ for $\eta=1$, and ~ 0.33 for $\eta=2$. The decrease in the power index n between the two phases is due to the slowing down of the particles outside the ML in the first vortex-free dispersion phase due to aerodynamic drag.

3.7 Afterburn of the Detonation Products

The afterburn of the detonation products is prominent in the ML , where they mix with the outer air and form products. The mass of $C(S)$ remaining in the charge, normalized with the initial charge mass, is presented in Figure 12 for four different cases, self-explanatory from the legend. The $C(S)$ mass fraction decreases rapidly at early times, as it comes in contact with the outer air for the first time; subsequently, the afterburn products (not to be confused with the detonation products) blanket out the inner detonation products and the outer air, and thus the sustenance of burning is limited to where the inner detonation products mix and react with the outer air, which is controlled by vorticity [2, 20, 21]. From Figure 12, the $C(S)$ mass fraction decay is nearly identical for $r_p=5$ and $10 \mu\text{m}$, i.e., is independent of particle size—a result proven very recently [2] (in [2], only $r_p > 10 \mu\text{m}$ were considered). Other observations from [2] that are also evident in Figure 12 are the higher afterburn observed for a higher mass loading ratio, and for a longer initial radial extent of the particle cloud.

While Figure 12 is useful to estimate the carbon mass remaining with time, also of interest is the rate of carbon mass remaining with time, for this illustrates the profile of the consumption rate of the fuel. To this end, the rate of mass of carbon remaining, normalized with the initial charge mass, is presented in Figure 13 for four cases considered hitherto, self-evident from the legend in Figure 13. As evident, the carbon consumption rates are sufficiently fast at early times ($t/t_o \sim 30$) as the detonation products and the air interact for the first time. Subsequently, the afterburn products blanket the inner detonation products and the outer air, thereby subdues the mixing between them—this decreases the carbon consumption rates.

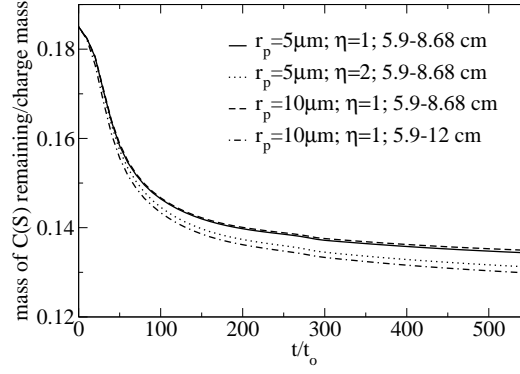


Figure 12. Carbon mass remaining with time, normalized with the initial charge mass.

Later, during the reshock phase ($t/t_o \sim 275$), the carbon consumption rates are locally enhanced owing to the enhanced mixing rates during the reshock phase—a consequence of the baroclinically generated vorticity. Upon close observation, the carbon consumption rates are nearly similar in time for $r_p=5$ and $10 \mu\text{m}$, showing near-independence to particle size. Also evident at early times is the higher carbon consumption rate for a wider initial particle cloud distribution, i.e., 5.9-12 cm versus 5.9-8.68 cm. These results conform to the observations made in [2].

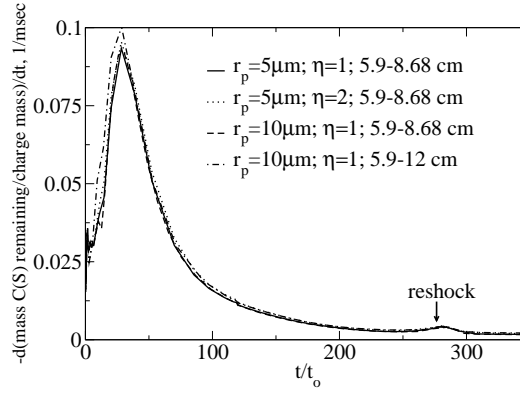


Figure 13. Rate of carbon mass remaining with time.

The afterburn of the detonation products and air is mixing-controlled, and how soon they mix is critical to the afterburn rates encountered. Thus, of preponderant interest here is to quantify the mixing process and investigate its variation with time. To this end, we define the quantity, “degree of mixedness,” denoted DM hereafter, similar to the definitions used elsewhere [28, 29], albeit for a binary and non-reacting system in these references. Specifically, we define DM as follows:

$$DM = \frac{\left[\frac{\int Y_{CO} (Y_{N_2} - Y_{N_2}^i) dV}{\int dV} \right]}{\left[\frac{\int Y_{CO} dV}{\int dV} \right] \left[\frac{\int (Y_{N_2} - Y_{N_2}^i) dV}{\int dV} \right]}, \quad (19)$$

where Y_{CO} and Y_{N_2} denote the instantaneous mass fractions of CO and N_2 , respectively, and $Y_{N_2}^i$ is the mass fraction of N_2 in the detonation products at the onset of detonation completion, obtained from the chemical balanced equation. Note that we use the quantity $Y_{N_2} - Y_{N_2}^i$ instead of Y_{N_2} , as N_2 is present on both sides of

the contact surface (more on the side of the air), and this difference represents only the “excess N_2 ” that belongs to the side of the air. Stated in these terms, the quantity DM will start from zero initially, as the inner CO and the excess N_2 are not yet mixed, and the quantity will increase as they mix subsequently. In Figure 14 (a), we study DM for $r_p=5\ \mu\text{m}$, and the initial cloud extending from $r=5.9$ - 8.68 cm, for $\eta=1$ and $\eta=2$. From Figure 14 (a), at early times, DM rapidly rises from zero to 0.03 as the species begin to mix. Subsequently, DM slightly decreases near $t/t_o \sim 12$, as the CO is consumed. Then, DM rises again during the implosion phase until about $t/t_o \sim 180$; DM is slightly greater for $\eta=2$ than for $\eta=1$, as more perturbations associated with the higher η result in enhanced hydrodynamic structures induced mixing. DM decreases during the reshock phase as the ML is compressed and, subsequently, increases again during the asymptotic phase at late times as the vorticity deposited in the ML during the reshock sustains the subsequent mixing process. Consequently, DM continues to be superior for the higher η . In Figure 14 (b), we study the dependence of DM on particle size and initial width of the cloud—the legend is self-explanatory. Whereas DM is independent of particle size (for $r_p=5$ and $10\ \mu\text{m}$), a wider initial cloud width ($r=5.9$ - 12 cm) results in a superior DM .

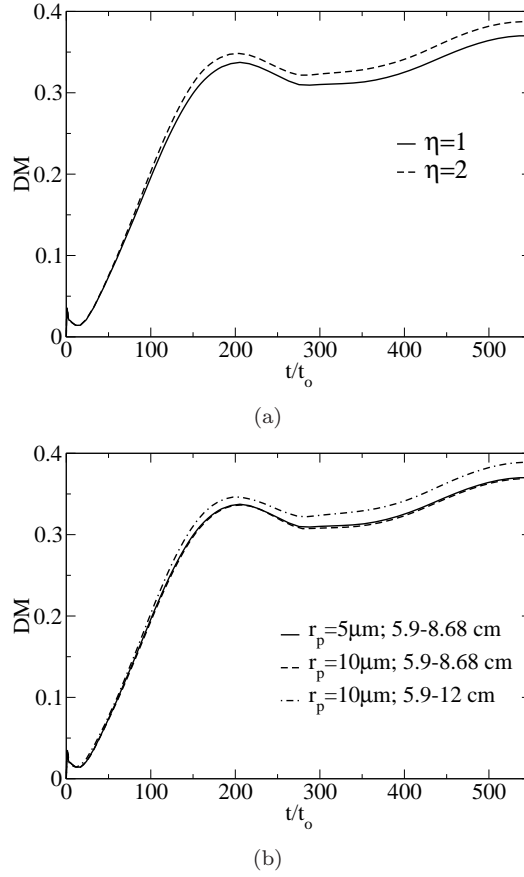


Figure 14. Degree of mixedness (DM): (a) effect of η ; (b) effect of r_p and initial cloud width.

3.8 Theoretical Hydrodynamic Considerations

The growth of hydrodynamic instabilities in classical gravity-driven fluid interfaces as well as blast wave driven systems alike, has been studied in the past using

many theoretical models; among these, the Buoyancy-Drag (BD) model is common [13, 30, 31]. In the BD model, the “rise” of bubbles is modeled accounting for buoyancy, drag, and decompression effects. The bubble amplitude (h) is obtained as [30]

$$\frac{d}{dt} \frac{dh(t)}{dt} = \tilde{A}g(t) - \frac{\tilde{C}}{\lambda} u_{inst}(t)^2 + \frac{d}{dt} \omega(t)h(t), \quad (20)$$

where \tilde{A} denotes the postshock-modified Atwood number $\tilde{A} = A(1 + \eta^*)/(C_a + \eta^*)$, where A is the post-shock Atwood number given by $A = (1 - \eta^*)/(1 + \eta^*)$, η^* is the post-shock density ratio, and C_a is the added mass coefficient and equals 2 for 2D and 1 for 3D. Furthermore, $g(t)$ denotes the driving acceleration, and \tilde{C} is the modified drag coefficient, given by the expression $\tilde{C} = C/(C_a + \eta^*)$, with C being the drag coefficient and equals $3 * 2\pi$ for 2D and $\approx 1.22 * 2\pi$ for 3D [30]. In addition, λ represents the perturbation wavelength, u_{inst} is the instability velocity, and $\omega(t)$ is the radial velocity gradient evaluated at the instantaneous interface, given as $\omega(t) = [\frac{\partial u(r,t)}{\partial r}]_{r=r_i(t)}$. Following the approach outlined in [30], the bubble amplitude is obtained as

$$\frac{dh}{dt} = u_{inst}(t) + \omega(t)h(t), \quad (21)$$

where the second term accounts for decompression effects. Substituting this into Equation (20), we obtain the standard BD equation

$$\frac{du_{inst}}{dt} = \tilde{A}g(t) - \frac{\tilde{C}}{\lambda} u_{inst}(t)^2. \quad (22)$$

In the current study, the BD analysis is carried out for the bubbles only, as we believe volumetric expansion effects due to chemical reactions, which is not accounted for in the present BD model, will be very significant for spikes as they are smaller (in terms of transverse length scale) than bubbles at the high Atwood numbers encountered in chemical explosions. We consider an ensemble of 10 bubbles from the simulation corresponding to $r_p=5 \mu\text{m}$, $\eta=1$ case (Case 1 in Table 1), and track the instantaneous amplitude (h) and transverse scale (L). The bubble amplitude is a measure of how much the bubble tip grows farther away from the 1D “unperturbed interface,” which is obtained from an additional single-phase, 1D unperturbed simulation. This 1D simulation is also used to evaluate the instantaneous interface radius ($r_i(t)$), $g(t)$ and $\omega(t)$ required for solving the BD equation (Equation (22)). Past studies using the BD model assume self-similar growth to obtain an amplitude dependent transverse length scale [28, 30]. We differ in the current analysis in the sense that self-similarity is not tacitly assumed; rather, it is demonstrated using the BD model. In our approach, transverse length scales from the 3D simulations are used as inputs to the BD model to estimate bubble amplitudes, which are then compared with the amplitudes obtained from the 3D simulations. First, the $L(t)$ for the bubble ensemble from the 3D simulations are used to compute $u_{inst}(t)$ from Equation (22), and from it $h(t)$ is evaluated using Equation (21). This analysis is performed using the initial amplitudes from $t/t_o \sim 12$ —approximately the time required for the contact surface to overtake the initial particle cloud—until $t/t_o \sim 160$ —the time when the secondary shock explodes

into the mixing layer during the reshock phase.

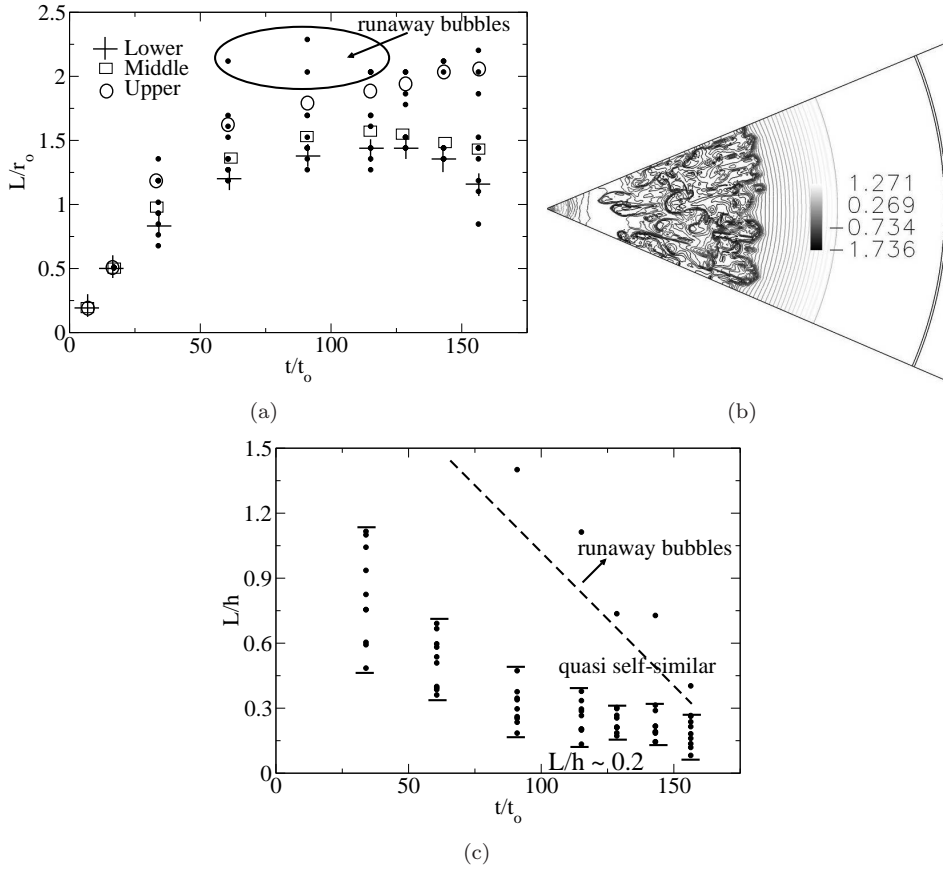


Figure 15. Bubble analysis from the 3D simulation for $\eta=1$, $r_p=5 \mu\text{m}$ and the initial particle cloud extending from $r=5.9\text{--}8.68 \text{ cm}$ (Case 1 in Table 1): (a) L ; (b) $\ln(\rho)$ contours at $t/t_0 \sim 130$ and (c) L/h . The bold dots in (a)&(c) denote the 3D simulation results.

Our simulation results show that a range of length scales exist for the bubbles, presented in Figures 15 (a)&(b), including some “runaway” [15] bubbles. Here, a “runaway” bubble is one which has grown significantly larger in size *vis-à-vis* its neighboring counterparts, and often tends to behave very differently than the other bubbles in the vicinity. A wide range of length scales exist for the bubbles, and this needs to be accounted for in the BD analysis. To this end, we classify the ensemble of bubbles into three branches—lower, middle and upper, and use three $L(t)$ curve-fits for the current analysis (all length scales are normalized with the initial charge radius, r_0). Of preponderant interest here is the self-similarity of bubbles at late times, a topic of wide debate in recent literature for Rayleigh-Taylor instability growth, albeit not previously studied for chemical explosions. By self-similarity, we refer to the growth of bubble amplitudes (h) proportional to their transverse scale (L). Based on our 3D simulations, the L/h ratio for the bubbles is presented in Figure 15 (c), and suggests $L/h \sim 0.8 \pm 0.3$ at early times, but tends to asymptote near $t/t_0 \sim 150$ to 0.2 ± 0.07 . Also, as evident, the “runaway” bubbles shown do not conform to self-similarity.

The asymptote behavior of L/h ratio essentially means that the “bubble competition” process terminates and the bubbles evolve with little or no memory of the initial length scales of the early perturbations. Such studies have been carried out in the past to supernovae and nuclear explosions, but not to chemical explosions to the best of the authors’ knowledge. At late times, the bubbles reach a “freeze-

out stage,” [28] i.e., no further merging occurs. The mode numbers (m) during this late time freeze-out stage is of preponderant interest; here, mode number is defined as $m = 2\pi r_i(t)/\lambda(t)$, where $r_i(t)$ denotes the instantaneous radial location of the interface. From [28], past simulations of supernovae explosions conform to freeze-out stage $m \sim 16$ -20; X-ray images of Cassiopeia A supernova shows $m \sim 20$; and high altitude nuclear explosions conform to freeze-out stage $m \sim 18$ -36. Our simulations predict freeze-out $m \sim 24$ -44 for the chemical explosions into ambient particle clouds. We believe that for systems that involve instantaneous perturbation followed by subsequent growth with no further external perturbations, freeze-out stage mode numbers may conform better to the predictions of [28], i.e., m up to 36. However, for chemical explosions into ambient particle clouds, the nature of the initial perturbations is not instantaneous, but rather lasts for a finite albeit small time—the time required for the contact surface to overtake the particle cloud. This prolonged initial forcing inevitably introduces additional perturbations during the first interaction event, which in turn correlates as marginally larger late time freeze-out stage mode numbers, m , up to 44.

The similarity ratio, L/h for the 3D simulation corresponding to $\eta=2$, $r_p=5 \mu\text{m}$ and the initial particle cloud extending from $r=5.9$ -8.68 cm (Case 2 in Table 1) is shown in Figure 16. As evident, L/h is nearly similar in value to the $\eta=1$ case (Figure 15 (c)) at early times. However, since more perturbations are introduced for $\eta=2$ during the first interaction event, the late time freeze-out stage L/h asymptotes to 0.27 ± 0.1 , indicating that there is partial retention of memory of the initial conditions at late times, i.e., the freeze-out L/h is not an “universal” value. Recent supernovae simulations also predict memory retention of the initial conditions at late times [30]. Furthermore, although there is this weak dependence of the initial conditions, the fact that L/h nearly asymptotes at late times for $\eta=1$ (Figure 15 (c)) and $\eta=2$ (Figure 16), indicates that a “quasi-self-similar growth” is possible for chemical explosions, where the transverse scale of the bubbles grows in proportion to its amplitude. However, this quasi-self-similar regime occurs only for a brief time instant, $t/t_o \sim 120$ -150, after which the reshock shrinks the hydrodynamic structures and deposits vorticity (baroclinic effect) which subsequently wrinkles/convolutes the structures. Due to the partial memory retention, the late time freeze-out stage photography of chemical explosions may contain some useful information on the nature of the initial perturbations. Our analysis shows that the reshock phase is faster for the $\eta=2$ case than $\eta=1$ by about $t/t_o \sim 5$; due to this earlier reshock for $\eta=2$, the secondary shock reaches the structures in the mixing layer around $t/t_o \sim 155$ and compresses them. Consequently, h decreases, causing an increase in L/h beyond $t/t_o > 150$, which is of no interest in the present study.

We apply the BD model for the ensemble of bubbles with the transverse length scale as input, and predict the amplitude growths with time. Critical to the BD model calculations is the definition of λ ; $\lambda=L$ has been used by some researchers [13], as well as $\lambda=2L$ by others [31]. To be precise, λ should be the ratio of the volume to cross-sectional area for the bubbles, which can be different for the bubbles depending on their shape. For instance, a “hemi-ellipsoidal bubble” can have a higher volume to cross-sectional area ratio than hemispherical bubbles. Both $\lambda=L$ and $\lambda=2L$ are used in the current analysis and the amplitudes (h) obtained from the BD model are presented in Figure 17 for the lower, middle and upper branches, along with the 3D simulation results. As evident, $\lambda=2L$ is in better accordance with higher amplitude bubbles, while $\lambda=L$ conforms to the smaller amplitude bubbles. During the implosion phase, our 3D simulation results show that small bubbles, albeit not all, implode deep into the core—increasing their amplitude, as shown in Figure 15 (b). These small bubbles have lesser drag and thus “rise” higher (higher

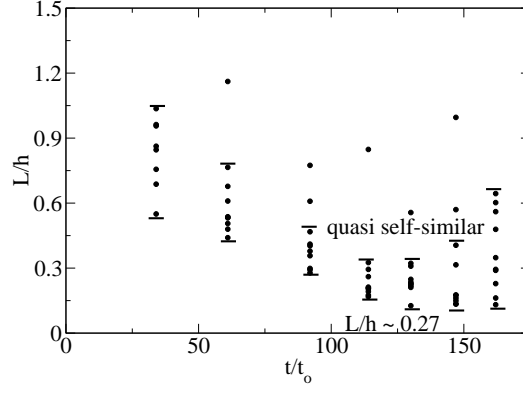


Figure 16. Bubble similarity from the 3D simulation for $\eta=2$, $r_p=5 \mu\text{m}$ and the initial particle cloud extending from $r=5.9\text{--}8.68 \text{ cm}$ (Case 2 in Table 1). The bold dots denote the 3D simulation results.

is actually deeper by convention), resulting in more oblong shapes that have high volume-to-area ratio; thus, as expected, the BD model predicts a higher amplitude for $\lambda=2L$. Larger bubbles, on the other hand, have a higher drag, which slows them as they try to “rise” away from the interface; thus, these bubbles have relatively smaller amplitudes, as also predicted by the BD model results. We believe that to properly characterize bubbles using the BD model, it is necessary to appropriately define bubble wavelengths (λ) based on their shapes. There is, however, limited work in literature on theoretical models with bubble shape-dependent wavelengths.

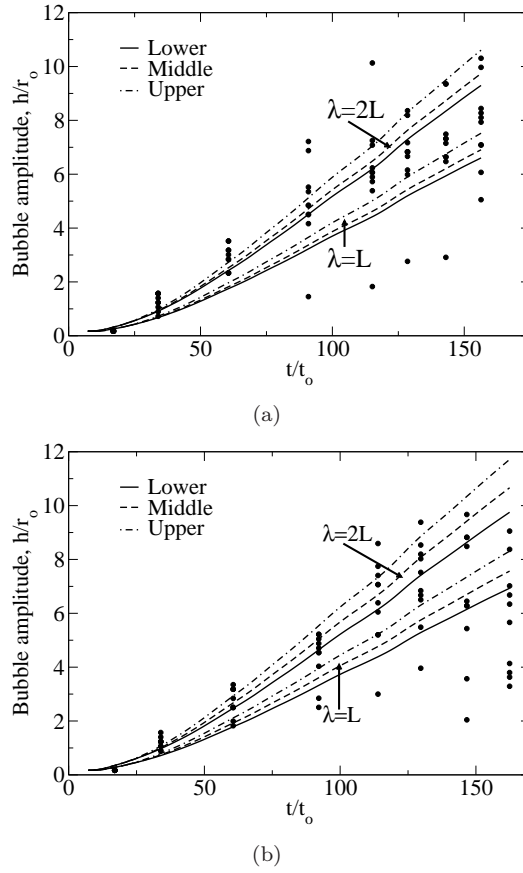


Figure 17. Bubble amplitudes obtained from the BD model for the case corresponding to (a) $\eta=1$, $r_p=5 \mu\text{m}$ and initial cloud extending from $r=5.9\text{--}8.68 \text{ cm}$ (Case 1 in Table 1); (b) $\eta=2$, $r_p=5 \mu\text{m}$ and initial cloud extending from $r=5.9\text{--}8.68 \text{ cm}$ (Case 2 in Table 1). The bold dots denote the 3D simulation results.

Also of interest is to predict the velocity with which the bubbles can “break-away” from the unperturbed interface. This is a direct measure of bubbles’ growth rates due to the forces acting on them, i.e., buoyancy and drag effects. In Equation (22), the first term represents the buoyancy term, and the second the drag effects; quantifying the effects of both these terms can be useful to investigate the effects of each of these terms. Figure 18 shows the instability velocities (u_{inst}) for the lower, middle and upper branches, for the simulation with $\eta=1$, $r_p=5\ \mu\text{m}$ and the initial particle cloud extending from $r=5.9\text{--}8.68\ \text{cm}$ (Case 1 in Table 1). The instability velocity presented here is normalized with r_o/t_o . As evident, the acceleration term (first term in Equation (22)) dominates at early times, with the bubbles reaching a non-dimensional terminal velocity of $\approx 0.025\text{--}0.03$ (this corresponds to a physical velocity of $\approx 200\ \text{m/s}$) at around $t/t_o \approx 30$. Subsequently, as the bubbles have grown to sufficiently large sizes (transverse scale), drag effects become more significant than the driving acceleration, thereby slowing down the bubbles. As evident from Figure 18, the bubbles slow down to $u_{inst}/(r_o/t_o) \approx 0.01$ at late times, i.e., just before the re-shock phase. This investigation demonstrates that theoretical models such as the currently employed Buoyancy-Drag model can be applied to directly obtain the bubble growth velocities and amplitudes; in addition, the terminal velocity of the bubbles can be determined using the BD model, which is useful for estimating the fireball dynamics from chemical explosions.

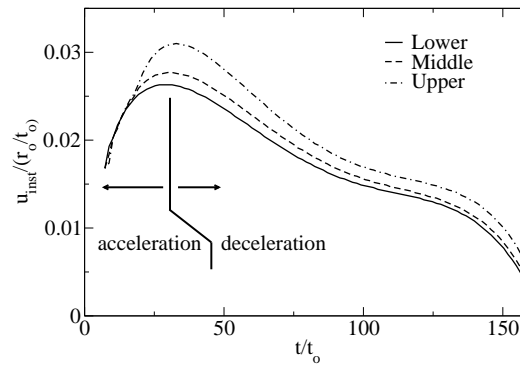


Figure 18. Bubble velocities predicted by the BD model for the case corresponding to $\eta=1$, $r_p=5\ \mu\text{m}$ and the initial particle cloud extending from $r=5.9\text{--}8.68\ \text{cm}$ (Case 1 in Table 1).

3.9 Preferential Particle Combustion

After the particles ignite during their early engulfment into the detonation products, their sustenance of burning depends on the clustering aspects. The vortex rings around the hydrodynamic structures bring into contact the inner detonation products and the outer air, and thereby sustains the afterburn of the detonation products. Thus, the local gas in the vortex rings are significantly hotter than the vortex-free regions, and so the particles that disperse through these vortex rings pick up more heat than their counterparts that do not. Consequently, preferential combustion of aluminum occurs, with the particles that pass through these vortex rings burning more.

To illustrate this preferential combustion/burning of particles, Figure 19 presents the particle temperature (Figures 19 (a) & (b)) and radius (Figures 19 (c) & (d)) at times $t/t_o \sim 25$ (Figures 19 (a) & (c)) and $t/t_o \sim 120$ (Figures 19 (b) & (d)). From Figure 19 (a), significant particle temperature gradients exist during this burning phase, as evident from the transitions between the red and green regions; this corresponds to the $t/t_o \sim 25$ time instant, when the particles are interacting

with the hydrodynamic structures in the *ML*—where afterburn occurs in regions dictated by where the inner detonation products and the outer air mix. At $t/t_o \sim 120$ (Figure 19 (b)), the particles have quenched, but temperature gradients still persist; however, note that after quenching, the range of particle temperatures has narrowed down *vis-à-vis* that during the earlier burning phase. Comparing the particle radii at these times (Figures 19 (c) & (d)), it is evident that the particles are relatively smaller in the regions where they are hotter, obviously due to the availability of heat from the afterburning regions of the *ML*. Thus, the burning characteristics of the particles are mixing-controlled, i.e., turbulent mixing plays a critical role in the burning of the aluminum particles.

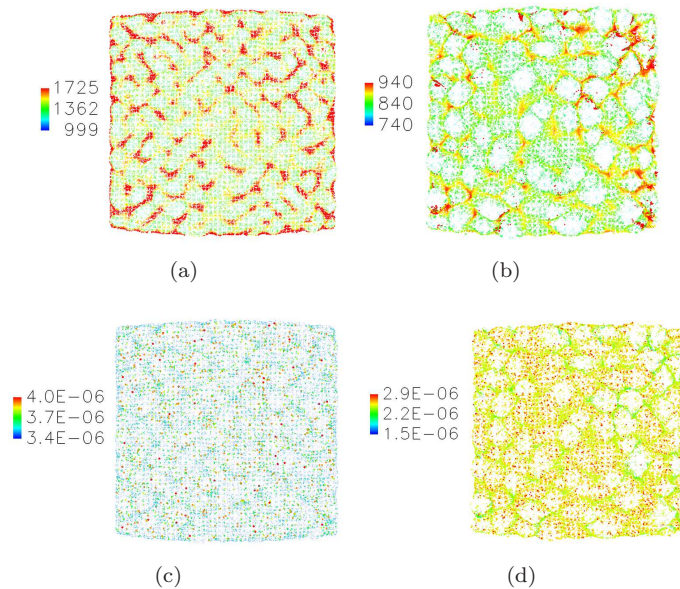


Figure 19. Preferential combustion of aluminum particles: particle temperature ((a) & (b)) and radius ((c) & (d)) at times $t/t_o \sim 25$ ((a) & (c)) and $t/t_o \sim 120$ ((b) & (d)). Temperature is in *Kelvin*, and radius is in *m*. The scales of the figures have been adjusted for better clarity.

3.10 Boundaries of Aluminum Combustion Products

Our observations show that aluminum particles, owing to their ignition during their engulfment into the detonation products, initially start to burn anaerobically; later, as the leading edge of the particle cloud enters the mixing layer, both aerobic and anaerobic burning concurrently occur; later, after all the particles leave the mixing layer, burning is strictly aerobic; subsequently, the particles quench. This transition between anaerobic to aerobic occurs gradually, and thus the different products of aluminum combustion exist in varying concentrations at different locations. Consequently, the oxides of aluminum (*AlO* and $Al_2O_3(L)$) exist in an annular region, similar to the aforementioned *ML*, i.e., they have a radial inner and outer boundaries; it is also of interest to investigate the motion of the exact region of this annular region where they exist. To study the region of existence of the aluminum oxides, and their convection with time, we present the boundaries of the aluminum oxides layer in Figure 20: inner boundary in Figure 20 (a) and outer boundary in Figure 20 (b). Here, we define the inner boundary of the aluminum oxide layer as the radial location where the azimuthally averaged mass fraction of *AlO* or $Al_2O_3(L)$, as the case may be, transitions from zero to 5% of the instantaneous maximum of the azimuthally averaged mass fraction of the respective aluminum

oxide. Likewise, the outer boundary is defined as where the transition is reversed, i.e., from 5% to zero of the respective aluminum oxidizer. Note that this definition is rather *ad hoc*, but does serve useful to portray a qualitative picture of the aluminum oxide layer. Furthermore, note that the region corresponding to AlO will be different from that of $Al_2O_3(L)$. Here, we consider the 5 and 10 μm particle radius, with $\eta=1$, and the initial cloud extending from $r=5.9$ -8.68 cm. The radius r (y -axis) is normalized with the initial charge radius, r_o . The profiles of AlO and $Al_2O_3(L)$ region boundaries, from Figures 20 (a) & (b), look similar qualitatively, as the detonation products-air ML .

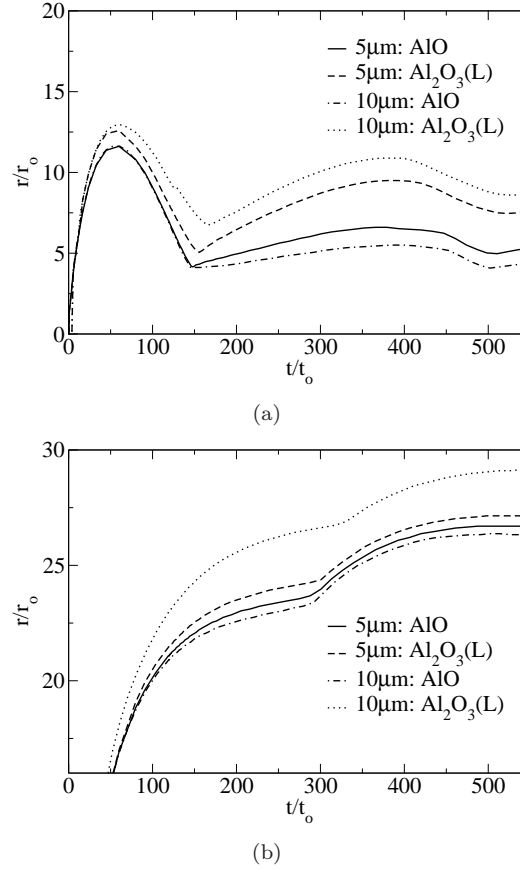


Figure 20. Boundaries of region of aluminum oxides (AlO , $Al_2O_3(L)$): (a) inner boundary; (b) outer boundary. Radius r is normalized with the initial charge radius, r_o .

As evident from Figure 20 (a), while the inner boundary of the AlO region is radially inside by $\sim 1.5r_o$ for the 10 μm size, it is outside by approximately the same distance for $Al_2O_3(L)$. Since the 10 μm radius particles have a higher inertia than the 5 μm particles, they spend a longer time engulfed into the detonation products. Consequently, when they ignite and burn, anaerobically to begin with, the AlO inner boundary is thus inside for the 10 μm radius particles. Due to the same reason, the 10 μm radius particles take a slightly longer time to reach the ML —the region where aerobic burning first occurs for the aluminum combustion; consequently, the inner boundary of the $Al_2O_3(L)$ region is also radially outside for the 10 μm particles. Note that once the particles pick up significant amounts of momentum from the gas they are set into motion, and will overtake the aluminum that was evaporated from them at earlier times by virtue of their higher inertia. Observing Figure 20 (b), whereas the outer boundary of the AlO region is only marginally inside for the 10 μm radius particles, it is significantly outside ($\sim 2r_o$)

for the outer boundary of the $Al_2O_3(L)$ region. Thus, for both aluminum oxides, the trends in the inner and outer boundaries conform to the fact that aluminum burning transitions smoothly (in time) from anaerobic to aerobic burning, irrespective of particle size.

4. Conclusions

A hybrid two-phase numerical methodology is used to study the flow-field behind turbulent explosions into an ambient dilute cloud of solid particles. Rayleigh-Taylor instabilities are observed at the contact surface and this grows in time into a mixing layer where the detonation products afterburn with the outer air. Five discernable phases of interest are identified in the particle dispersion: (1) engulfment phase; (2) hydrodynamic instability-interaction phase; (3) first vortex-free dispersion phase; (4) reshock phase; and (5) second vortex-free dispersion phase. As the particles disperse radially outwards, they interact with the vortex rings around the Rayleigh-Taylor structures in the mixing layer, which introduces transverse velocity components to the particles, causing them to cluster. Later, the particles leave the mixing layer, yet preserve their clustered shape or hydrodynamic “foot print.” A higher mass loading ratio of the initial cloud results in larger and fewer clusters; a larger particle size tends to form fewer and diffuse clusters when the initial particle cloud is wider. Preferential heating and combustion is observed in the particle cloud due to the clustering effects. Later, the secondary shock reshocks the mixing layer, resulting in a Richtmyer-Meshkov instability; subsequently reshocks the particle cloud.

A theoretical analysis of the “bubble” growth is undertaken using the Buoyancy-Drag model, and the amplitude predictions are in reasonable agreement with the simulation results. Furthermore, a quasi-self-similar regime is observed where the bubble transverse scales grow in proportion to the amplitude, although this regime lasts only for a small time interval. The ratio of the transverse length scale to amplitude during this quasi-self-similar regime is slightly higher when the initial particle cloud is wider, signifying partial memory retention of the initial perturbations for explosions into ambient particle clouds. Overall, this study has provided some useful insights on the ignition and clustering of dilute aluminum particle clouds upon explosive dispersal, and on the hydrodynamic characterization of turbulent explosions.

5. Acknowledgements

This research is supported by the Office of Naval Research (Dr. Cliff Bedford, Program Manager), the Air Force Research Laboratory, Eglin Air Force Base (Dr. Douglas V. Nance, Program Manager), and the Air Force Office of Scientific Research (Dr. Fariba Fahroo, Program Manager). Simulations were carried out at the DoD HPC Centers at the U.S. Army Research Laboratory Major Shared Resource Center and the Maui High Performance Computing Center. Dr. Douglas V. Nance supplied the initial detonation profiles. The first author acknowledges the brief private communications with Dr. Aaron Miles of the Lawrence Livermore National Laboratory.

References

- [1] K. Balakrishnan, F. Genin, D. V. Nance, and S. Menon, *Numerical study of blast characteristics from detonation of homogeneous explosives*, Shock Waves 20(2) (2010), pp. 147-162.
- [2] K. Balakrishnan, and S. Menon, *On the role of ambient reactive particles in the mixing and afterburn behind explosive blast waves*, Combust. Sci. and Tech. 182(2) (2010), pp. 186-214.
- [3] K. Balakrishnan, D. V. Nance, S. Menon, *Simulation of impulse effects from explosive charges containing metal particles*, Accepted for publication in Shock Waves (2010), DOI: 10.1007/s00193-010-0249-z.
- [4] T. Bazyn, H. Krier, and N. Glumac, *Evidence of the transition from the diffusion-limit in aluminum particle combustion*, Proc. Combust. Instit. 31 (2007), pp. 2021-2028.
- [5] M. W. Beckstead, *Correlating aluminum burning times*, Combust., Expl. and Shock Waves 41 (2005), pp. 533-546.
- [6] K. Benkiewicz, and A. K. Hayashi, *Parametric studies of aluminum combustion model for simulations of detonation waves*, AIAA J. 44(3) (2006), pp. 608-619.
- [7] H. L. Brode, *Blast wave from a spherical charge*, The Phys. of Fluids 2 (1959), pp. 217-229.
- [8] S. Chandrasekhar, *Hydrodynamic and Hydromagnetic Stability*, Oxford University Press, 1961.
- [9] R. Chein, and J. N. Chung, *Effects of vortex pairing on particle dispersion in turbulent shear flows*, Int. J. Multiphase Flow 13(6) (1987), pp. 785-802.
- [10] R. Chein, and J. N. Chung, *Simulation of particle dispersion in a two-dimensional mixing layer*, AIChE J. 34 (1988), pp. 946-954.
- [11] R. Clift, J. R. Grace, and M. E. Weber, *Bubbles, Drops and Particles*, Academic, New York, 1978.
- [12] C. Crowe, M. Sommerfeld, and Y. Tsuji, *Multiphase Flows with Droplets and Particles*, CRC Press, 1998.
- [13] G. Dimonte, and M. B. Schneider, *Turbulent Rayleigh-Taylor instability experiments with variable acceleration*, Phys. Rev. E 54 (1996), pp. 3740-3743.
- [14] F. Genin, and S. Menon, *Dynamics of sonic jet injection into supersonic crossflow*, Accepted for publication in J. of Turbulence (2009).
- [15] J. Glimm, O. McBryan, R. Menikoff, and D. H. Sharp, *Stable and runaway bubble merger in a model for Rayleigh-Taylor unstable interfaces*, Phys. Letters A 123 (1987), pp. 289-292.
- [16] S. Gordon, and B. J. McBride, *Computer program for calculation of complex chemical equilibrium compositions and applications: I. analysis*, NASA Reference Publication 1311 (1994).
- [17] I. A. Johnston *The Noble-Abel equation of state: thermodynamic derivations for ballistics modelling*, Defence Sci. and Tech. Org., DSTO-TN-0670 (2005).
- [18] A. Khasainov, and B. Veyssiere, *Steady, plane, double-front detonations in gaseous detonable mixtures containing a suspension of aluminum particles*, Dyn. of Expl.: Prog. in Astro. and Aero. 114 (1988), pp. 284-298.
- [19] C. K. Kim, J. G. Moon, J. S. Hwang, M. C. Lai, and K. S. Im, *Afterburning of TNT explosive products in air with aluminum particles*, AIAA Paper 2008-1029 (2008).
- [20] A. L. Kuhl, *Spherical Mixing Layers in Explosions*, Dyn. of Exothermicity, Gordon and Breach Publishers (1996), pp. 291-320.
- [21] A. L. Kuhl, R. E. Ferguson, and A. K. Oppenheim, *Gasdynamic model of turbulent exothermic fields in explosions*, Prog. in Astro. and Aero. 173 (1997), pp. 251-261.
- [22] A. L. Kuhl, P. Neuwald, and H. Reichenbach, *Effectiveness of combustion of shock-dispersed fuels in calorimeters of various volumes*, Combust., Expl. and Shock Waves 42 (2006), pp. 731-734.
- [23] E. Leinov, G. Malamud, Y. Elbaz, L. A. Levin, G. Ben-Dor, D. Shvarts, and O. Sadot, *Experimental and numerical investigation of the Richtmyer-Meshkov instability under re-shock conditions*, J. Fluid Mech. 626 (2009), pp. 449-475.
- [24] W. Ling, J. N. Chung, T. R. Troutt, and C. T. Crowe, *Direct numerical simulation of a three-dimensional temporal mixing layer with particle dispersion*, J. Fluid Mech. 358 (1998), pp. 61-85.
- [25] P. Lynch, H. Krier, and N. Glumac, *A correlation for burn time of aluminum particles in the transition regime*, Proc. Combust. Instit. 32 (2009), pp. 1887-1893.
- [26] P. Lynch, H. Krier, and N. Glumac, *Size distribution effects in heterogeneous shock tube burntime experiments*, AIAA Paper 2009-5053 (2009).
- [27] S. Menon, and N. Patel, *Subgrid modeling for simulation of spray combustion in large-scale combustors*, AIAA J. 44(4) (2006), pp. 709-723.
- [28] A. R. Miles, *Bubble merger model for the nonlinear Rayleigh-Taylor instability driven by a strong blast wave*, Phys. of Plasmas 11(11) (2004), pp. 5140-5155.
- [29] A. R. Miles, et al., *Transition to turbulence and effect of initial conditions on three-dimensional compressible mixing in planar blast-wave-driven systems*, Phys. of Plasmas 12(5) (2005), pp. 056317-056317-10.
- [30] A. R. Miles, *The blast-wave-driven instability as a vehicle for understanding supernova explosion structure*, The Astroph. J. 696 (2009), pp. 498-514.
- [31] D. Oron, L. Arazi, D. Kartoon, A. Rikanati, U. Alon, and D. Shvarts, *Dimensionality dependence of the RayleighTaylor and RichtmyerMeshkov instability late-time scaling laws*, Phys. Plasmas 8(6) (2001), pp. 2883-2889.
- [32] R. D. Richtmyer, *Taylor instability in a shock acceleration of compressible fluids*, Comm. on Pure and Appl. Math. 13 (1960), pp. 297-319.
- [33] D. A. Schwer, and K. Kailasanath, *Numerical simulation of the mitigation of unconfined explosions using water-mist*, Proc. Combust. Instit. 31 (2007), pp. 2361-2369.
- [34] L. I. Sedov, *Similarity and Dimensional Methods in Mechanics*, Academic Press, 1959.
- [35] K. D. Squires, and J. K. Eaton, *Preferential concentration of particles by turbulence*, Phys. Fluids A 3(5) (1991), pp. 1169-1178.
- [36] V. Tanguay, S. Goroshin, A. J. Higgins, and F. Zhang, *Aluminum particle combustion in high-speed detonation products*, Combust. Sci. and Tech. 181 (2009), pp. 670-693.
- [37] G. I. Taylor, *The formation of a blast wave by a very intense explosion*, Proc. of the Royal Soc. of

- London 201(1065) (1950), pp. 159-174.
- [38] G. I. Taylor, *The instability of liquid surfaces when accelerated in a direction perpendicular to their planes*, Proc. of the Royal Soc. of London. Series A, Math. and Phys. Sci. 201 (1950), pp. 192-196.
 - [39] E. F. Toro, *Riemann Solvers and Numerical Methods for Fluid Dynamics*, Springer, 1999.
 - [40] L. A. Vulis, *Thermal Regimes of Combustion*, McGraw Hill Book Company, New York, 1961.
 - [41] S. Xu, T. Aslam, and D. S. Stewart, *High resolution numerical simulation of ideal and non-ideal compressible reacting flows with embedded internal boundaries*, Combust. Theo. and Model. 1 (1997), pp. 113-142.
 - [42] S. Xu, and D. S. Stewart, *Deflagration-to-detonation transition in porous energetic materials: a comparative model study*, J. of Eng. Math. 31 (1997), pp. 143-172.
 - [43] F. Zhang, J. Anderson, and A. Yoshinaka, *Post-detonation energy release from TNT-aluminum explosives*, AIP Shock Compression of Condensed Matter, Waikoloa, Hawaii, 2007.